Characterization of the optical properties of complex aerosol mixtures observed with a multiwavelength–Raman–polarization lidar during the 6–weeks BACCHUS campaign in Cyprus in spring 2015

Masterarbeit

zur Erlangung des akademischen Grades

Master of Science

vorgelegt von
Clara Kaduk
Matrikelnummer 2143166

Fakultät für Physik und Geowissenschaften
der Universität Leipzig
Studiengang Meteorologie

Erstgutachter: Prof. Dr. A. Macke
Leibniz-Institut für Troposphärenforschung (TROPOS)
Zweitgutachter: Jun.-Prof. Dr. B. Pospichal
Institut für Geophysik und Meteorologie, Universität zu Köln
Betreuer: Dr. Albert Ansmann, Dr. Holger Baars (TROPOS)

12.07.2017

Table Of Contents

1 Introduction **1**

2 Cyprus: Meteorological Conditions, Fire Activity, Dust Outbreaks and Previous Aerosol Research **4**

2.1 Meteorological Conditions 4

2.1.1 Climate of Cyprus 4

2.1.2 Meteorological Conditions in March and April 2015 at Nicosia, Cyprus 5

2.2 Fire Activity and Dust Outbreaks 7

2.3 Previous Aerosol Research 12

3 BACCHUS–Cyprus campaign **14**

3.1 Overview 14

3.2 Polly^{XT} 16

4 Methodology **19**

4.1 Lidar 19

4.1.1 Lidar equation 20

4.1.2 Klett–Method 21

4.1.3 Raman–Lidar–Method 21

4.2 Aerosol optical properties 23

5 Results – Part I: Case Studies **28**

5.1 Case Study: March 7, 2015 31

5.2 Case Study: March 9, 2015 36

5.3 Case Study: April 7, 2015 39

5.4 Case Study: April 9, 2015 42

5.5 Discussion 44

6 Results – Part II: Statistical Analysis **46**

6.1 Overview 46

6.2 Time Series 49

6.3 Aerosol Characterization 55

7 Conclusion and Outlook **63**

Bibliography **65**

List of Figures **70**

List of Tables **72**

List of Abbreviations **73**

Selbstständigkeitserklärung **75**

Chapter 1

Introduction

Aerosols are an important player in the global climate system. According to the Fifth Assessment Report of the Intergovernmental Panel on Climate Change, aerosol–cloud interactions still pose the largest uncertainty to estimates of the Earth's changing energy budget (IPCC 2013). Aerosols affect the Earth's energy budget directly and indirectly. The aerosol direct effect describes the influence of aerosols by scattering and absorbing radiation. The aerosol indirect effect describes the influence of aerosols on clouds. Aerosols can change the cloud droplet concentration and droplet size and thus the cloud radiative properties (IPCC 2007). They also influence the amount and lifetime of clouds acting as cloud condensation nuclei (CCN). In the case of liquid water clouds a high aerosol concentration favors the formation of more but smaller droplets compared to an environment with less CCN available. Many small droplets have a greater reflecting surface than a few bigger droplets, which results in an increased reflection of solar radiation. This effect is the so–called Twomey effect (Twomey 2007). The cloud droplet concentration itself affects the lifetime of clouds and the intensity of precipitation. Bigger droplets have a higher probability of raining out compared to smaller droplets and thus reduce the lifetime of clouds (Albrecht 1989).

The influence of aerosols on ice formation in clouds is a complex topic. Aerosol particles can serve as ice nuclei (IN) and facilitate ice formation, which is called heterogeneous ice formation (Seifert 2010).

The sign and magnitude of the radiative forcing of aerosols depend on the aerosol type, the vertical distribution and the presence of clouds underneath the aerosol layers. Since these components are highly variable, aerosols can have strong effects on the regional climate. A good knowledge of the aerosol conditions is necessary for a reliable estimation of the aerosol effects in the climate system.

The measurement instrument lidar (light detection and ranging) is an appropriate tool to observe the vertical aerosol structure. It is an active remote sensing instrument that makes use of the effects of atmospheric scattering and absorption of light to gain information on the state and composition of the atmosphere. Recent developments of small compact lidars make it possible to perform automated unattended measurements at even remote locations (Engelmann et al. 2016). The portable lidar Polly was developed at the Leibniz Institute for Tropospheric Research in Leipzig (TROPOS) in 2003. Since then various campaigns took place and several Polly active stations have been established (Baars et al. 2011, 2015; Engelmann et al. 2016).

One recent campaign was the BACCHUS–Cyprus campaign in spring 2015. During six weeks, measurements with different instruments were performed, including observations with the multiwavelength–Raman–polarization lidar Polly$^{\mathrm{XT}}$.

Cyprus is located in the Eastern Mediterranean and already exhibits Middle East climate conditions with prevailing dry and hot weather. The island is located in one of the most polluted areas in the world (Weinzierl 2014). A mixture of different aerosol types can be found: dust from the Saharan desert and deserts in the Middle East, smoke from the North and anthropogenic pollution from urban industrial conglomerations in southeastern Europe (Nisantzi et al. 2014, 2015). Since Cyprus is an island, marine aerosols also play an important role.

Figure 1.1: Aerosol transport to Cyprus [adapted from *Weinzierl*, 2014]

The transport of the different aerosol types to Cyprus can be seen in Figure 1.1.
Cyprus and the region around can serve as an exciting and ideal natural laboratory for atmospheric and climate research. It offers unique opportunities for the study of aerosols and their interaction with clouds. The area is also recognized as a hot spot for climate change (Weinzierl 2014).

The presented work deals with the aerosol conditions in the region around Cyprus. The BACCHUS–Cyprus campaign, particularly the measurements with the multiwavelength–Raman–polarization lidar Polly^{XT} will be discussed regarding instrumentation, data analysis and observed aerosol optical properties.

After this introduction, Chapter 2 will give an overview of the meteorological conditions, fire activity, dust outbreaks and previous aerosol research in Cyprus. In Chapter 3, the BACCHUS–Cyprus campaign and the multiwavelength–Raman–polarization lidar Polly^{XT} will be introduced. Chapter 4 deals with the methodology, including the lidar principle and the gain of the aerosol optical properties. The results of the experiment will be presented in Chapter 5 and 6. In Chapter 5, several case studies will be discussed, whereas Chapter 6 presents a detailed statistical analysis of the aerosol conditions in Cyprus during the experiment. A conclusion and an outlook will be given in Chapter 7.

Chapter 2

Cyprus: Meteorological Conditions, Fire Activity, Dust Outbreaks and Previous Aerosol Research

This chapter gives an overview of the meteorological conditions in Cyprus and shows under which circumstances the experiment took place. Dust outbreaks and fire activity in the area around Cyprus are discussed. Furthermore, findings from previous campaigns are shown.

2.1 Meteorological Conditions

This section starts with a characterization of the climate of Cyprus including average annual precipitation, temperature differences and winds, followed by a detailed description of the meteorological conditions during the experiment in Nicosia in March and April 2015. General information on Cyprus regarding weather and climate can be found on the webpage of the Department of Meteorology Cyprus, a department under the administration of the Ministry of Agriculture, Rural Development and Environment (MOA, www.moa.gov.cy).

2.1.1 Climate of Cyprus

The climate of Cyprus is described as "intense Mediterranean" with a typical seasonal rhythm marked in respect of temperature, rainfall and weather (MOA 2017b). Summers from mid–May to mid–September are hot and dry, whereas winters from November to mid–March are rainy and rather changeable. Short autumn and spring seasons with rapid changes of the weather conditions appear. A shallow trough of low pressure extending from the great continental depression centered over southwest Asia affects Cyprus in summer.

High temperatures and almost cloudless skies appear. Between the continental anticyclone of Eurasia and the generally low pressure belt of North Africa fairly frequent small depressions cross the Mediterranean Sea from west to east in winter. For Cyprus these depressions mean periods of disturbed weather usually lasting from one to three days. Most of the annual precipitation is produced in these days, the average rainfall from December to February is about 60 % of the annual total.
The meteorology of Cyprus is strongly affected by the central Troodos massif (up to 1951 m) and the Kyrenia mountain range (peaks up to 1000 m). Orographic lift can cause clouds and precipitation and on the other hand strong leeward winds. The average annual precipitation is about 1100 mm at the top of the central massif. On the leeward slopes the amount decreases steadily northwards and eastwards to between 300 and 350 mm in the central plain and the flat southeastern parts of the island and on the windward slopes to 450 mm in the southwest.
Regarding air temperature, the seasonal difference between mid–summer and mid–winter temperatures is quite large with 18 °C inland and about 14 °C on the coasts. Differences between day maximum and night minimum temperatures are also quite large. In winter these differences are 8 to 10 °C on the lowlands and 5 to 6 °C on the mountains increasing in summer to 16 °C on the central plain and 9 to 12 °C elsewhere.
Winds are quite variable in direction with orography and local heating effects playing an important role in determining local wind direction and strength. Over the eastern Mediterranean, surface winds are mostly westerly or southwesterly in winter and northwesterly or northerly in summer. They are usually of light or moderate strength. Considerable sea and land breezes, mainly occuring in periods of clear skies in summer, are not only marked near the coasts, but also regularly penetrate far inland reaching the capital Nicosia. They often bring along a reduction of temperature and also an increase in humidity.

2.1.2 Meteorological Conditions in March and April 2015 at Nicosia, Cyprus

According to the meteorological reports for March and April 2015 (see Figure 2.1), provided by the Meteorological Service of Cyprus, the weather in March 2015 was "relatively warm" and in April 2015 "relatively dry and cold"(MOA 2017c).

The mean maximum air temperature in Nicosia (Greek: Lefkosia) was with 19.6 °C slightly above the normal value for March (normal period 1971–2000). The same applies to the mean minimum air temperature of 8.2 °C for March 2015. A highest value for the air temperature of 27.0 °C was found and a lowest value of 4.2 °C.

METEOROLOGICAL REPORT FOR MARCH 2015

Stations	Height above M.S.L. (m)	Air Temperature (°C)				Relative Humidity %		Rainfall (mm)				
		Mean Max.	Mean Min.	Highest Max.	Lowest Min.	0600 G.M.T.	1100 G.M.T.	Total Amount	No. of Rain days	Greatest Amount in 24 hrs	Date	No. of Snow days
Lefkosia (Athalassa)	162	19.6	8.2	27.0	4.2	72	49	49.9	11	24.7	11	-

DIFFERENCE FROM NORMAL FOR MARCH 2015

Stations	Barometric Pressure M.S.L. (hPa)		Air Temperature (°C)						Rainfall (mm)	
	Pressure	Difference from Normal	Mean Max.	Difference from Normal	Mean Min.	Difference from Normal	Mean Temp.	Difference from Normal	Total for month	Difference from Normal
Lefkosia (Athalassa)	1016.7	+1,7	19,6	+1,0	8,2	+1,8	13,9	+1,4	49,9	+12,9
Larnaka Airport	1016.7	+1,8	20,5	+1,8	9,8	+1,6	15,1	+1,6	65,1	+26,1

Normal Period for Temperature : 1971 - 2000
Normal Period for Rainfall : 1961 - 1990

METEOROLOGICAL REPORT FOR APRIL 2015

Stations	Height above M.S.L. (m)	Air Temperature (°C)				Relative Humidity %		Rainfall (mm)				
		Mean Max.	Mean Min.	Highest Max.	Lowest Min.	0600 G.M.T.	1100 G.M.T.	Total Amount	No. of Rain days	Greatest Amount in 24 hrs	Date	No. of Snow days
Lefkosia (Athalassa)	162	23.1	9.6	34.1	6.2	55	34	13.1	3	7.9	10	-

DIFFERENCE FROM NORMAL FOR APRIL 2015

Stations	Barometric Pressure M.S.L. (hPa)		Air Temperature (°C)						Rainfall (mm)	
	Pressure	Difference from Normal	Mean Max.	Difference from Normal	Mean Min.	Difference from Normal	Mean Temp.	Difference from Normal	Total for month	Difference from Normal
Lefkosia (Athalassa)	1014.3	+ 1,1	23,1	- 1,2	9,6	- 0,5	16,3	- 0,9	13,1	- 8,9
Larnaka Airport	1014.4	+ 1,4	22,3	- 0,1	11,0	- 0,4	16,7	- 0,2	11,5	- 6,5

Normal Period for Temperature : 1971 - 2000
Normal Period for Rainfall : 1961 - 1990

Figure 2.1: Meteorological Reports for March and April 2015 for Lefkosia (Nicosia), Cyprus [adapted from *MOA*, 2017]

The rainfall amount at Nicosia was much higher than the normal value (normal period 1961–1990), reaching 49.9 mm during 11 days of rain.
In April 2015, the air temperature in Nicosia was little below normal with a mean maximum air temperature of 23.1 °C and a mean minimum air temperature of 9.6 °C. A highest value of 34.1 °C and a lowest value of 6.2 °C was found. With only 3 days of rain and a total amount of 13.1 mm, the rainfall was clearly weaker than normal.

2.2 Fire Activity and Dust Outbreaks

The island of Cyprus has to deal with a high risk of forest fires. High temperatures, prolonged drought periods and the extremely flammable vegetation facilitate the ignition and spreading of forest fires particularly in summer. The months June and July are considered as most risky months according to forest fire statistics (MOA 2017a). During the experiment in March and April 2015, no forest fires were detected in Cyprus. But not only fires in the immediate environment play a role for the aerosol conditions in Cyprus. During fires, air parcels are released with a very high temperature compared to the surrounding air temperature. Due to buoyancy, these air parcels can easily rise to high altitudes. As a consequence, a large amount of smoke particles reaches the free troposphere and can be transported over large distances.

Figure 2.2 shows locations of fires detected by MODIS (Moderate Resolution Imaging Spectrometer) on board the Terra and Aqua satellites in March and April 2015, accumulated over a 10–day period. The images were created with MODIS Active fire data (Collection 5) using FIRMS Web Fire Mapper provided by NASA (https://firms.modaps.eosdis.nasa.gov/firemap/ 2017). Each colored dot indicates a location where MODIS detected at least one fire during the compositing period.

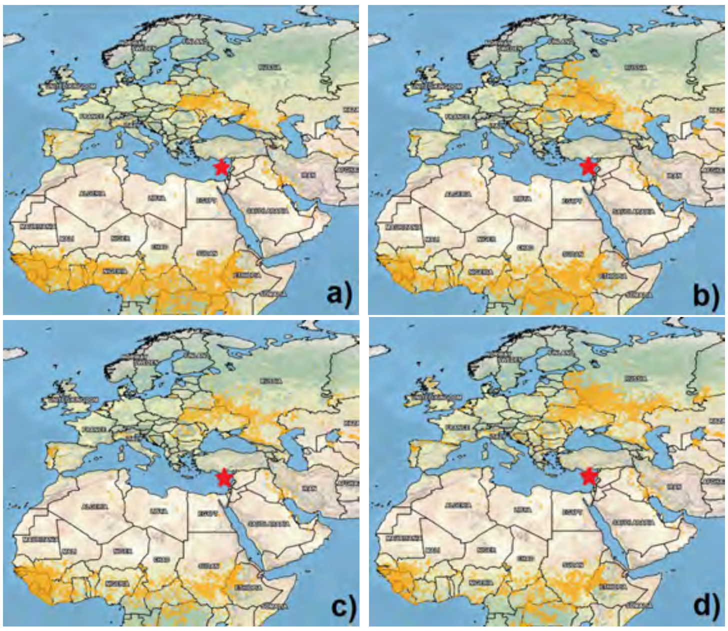

Figure 2.2: Fire Activity (yellow dots) in the region around Cyprus (red star). 10–day periods: a) 03.03.–13.03.2015, b) 14.03.–24.03.2015, c) 25.03.–04.04.2015, d) 05.04.–15.04.2015. (https://firms.modaps.eosdis.nasa.gov/firemap/)

During the BACCHUS–Cyprus campaign in March and April 2015, a huge amount of fires was detected in the northeast, north and northwest of the Black Sea, affecting the Ukraine, Romania, Belarus and southern parts of Russia. Forest fires at this time of the year are common in these regions, but the amount of fires appears to be higher compared to the preceding years. This can probably be attributed to the Ukraine crisis, that already started in spring 2014 and still couldn't find an end. After the 2nd Minsk–Contract in February 2015, that called for the withdrawal of heavy weapons from the frontline, attacks had fallen, but the activity of sniper groups increased and rebels continued to fire on government positions (ARD 2015; UCMC 2015; Reuters 2015). A similar situation took place in Iraq, where strong fires were detected during the entire experiment in March and April 2015. Since January 2014, Iraq is engaged in civil war with a huge amount of severe battles including the "Second Battle of Titris" in March 2015 and the "Al–Karmah offensive" in April 2015 (BBC 2015; Huffingtonpost 2015; IRAQINEWS 2015). More heavy fires were detected by MODIS in West, Central and East Africa. Especially in Sierra Leone, located between Guinea, Liberia and the Atlantic Ocean, the frequency of agricultural burning was high (NASA 2015). Few fires were detected in Southwestern Europe and North Africa. Occasional fires appeared in Western, Eastern and Central Europe, as well as in Turkey. In the end of the campaign (Figure 2.2 d), the fire activity in Eastern and Southeastern Europe increased, whereas African fires decreased.

Not only smoke particles, but also mineral dust can be transported over large distances and affect the aerosol conditions in Cyprus. In the region around Cyprus, two main areas appear as dust sources: the Saharan desert and deserts in the Middle East (see Figure 2.3).

The Saharan desert is the world's largest mineral dust source (Washington et al. 2003). From there, mineral dust is spread all over the globe, across the Mediterranean Sea towards Europe and Western Asia and across the tropical North Atlantic Ocean as far as the Caribbean and South America. The Bodélé Depression between Tibesti and Lake Chad (south central Sahara) is the most intense dust source, followed by a large but less intense area in the west Sahara and Libya (Washington et al. 2003). Further important dust sources can be found in Mauritania, Mali, southern and northeastern Algeria and Tunisia (Washington et al. 2003). Most of the prominent sources are associated with topographical lows or with regions on the flanks of topographical highs. Some of the most active dust sources in North Africa border on the Ahaggar and Tibesti Mountains (Prospero et al. 2002). The latter include the highest point in the Sahara and are located in the north of Chad with a small extension into southern Libya.

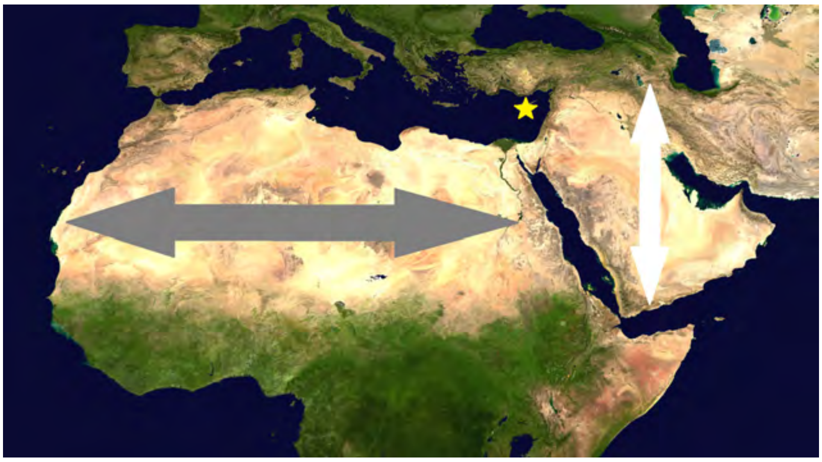

Figure 2.3: Map section showing southern and southeastern europe, the northern part of Africa and the Arabian Peninsula. Dust sources in the region around Cyprus (yellow star) are indicated by arrows: The Saharan Desert (grey arrow) and deserts in the Middle East (white arrow). Map source: http://earthobservatory.nasa.gov.

This indicates the important role of weathering processes and runoff from the mountains in providing fine soil material that can be mobilized as dust (Prospero et al. 2002). Longe–range dust transport from the Sahara can be effected in an easterly jet covering a broad area of the Sahara including North Sudan, Chad, and Niger, as well as South Egypt and Libya (Washington et al. 2003).

The deserts of the Arabian Peninsula are among the most important and persistent dust sources worldwide (Ginoux et al. 2012). In particular, the Arabian Peninsula is a source of intense dust storms with an important contribution to the long–range transport of mineral aerosols over the Indian Ocean (Rajeev et al. 2000) and adjacent regions (e.g. the Arabian Sea and Iran) (Zhu et al. 2007). The maximum of dust storm activity is identified over eastern and central Saudi Arabia (Ad Dahna Desert) as well as the Saudi–Oman border (Rub al Khali or Empty Quarter Desert) during the summer months (Washington et al. 2003). Over the Arabian Peninsula, dust storms develop throughout the year, following a distinct annual cycle with low activity during winter, strengthening between March and April, reaching a maximum during June and July (Prospero et al. 2002). Prospero et al. (2002) also identified the areas of the eastern coast of the Persian Gulf, Oman and southern Iraq as regions of intense dust storm activity. While dust emission and resuspension is controlled by microscale processes, intense dust storms (i.e. in terms of total airborne mass, spatial extent, and duration) require strong and/or persistent wind conditions driven by meso– to synoptic–scale mechanisms.

Frequently, dust storms in the Middle East are related to the postfrontal regime of midlatitude low pressure systems propagating eastward, also known as the winter Shamal wind (Rao et al. 2001). Prefrontal winds (named 'Kaus' in Saudi Arabia) can also trigger strong dust outbreaks (Hamidi et al. 2013).

Based on MODIS satellite images, generated with NASA Worldview (https://worldview.earthdata.nasa.gov 2017), several dust outbreaks from the Middle East and the Sahara were identified in March and April 2015. For this purpose, the layer 'Corrected Reflectance (True Color)' was applied, showing natural–looking images of land surface, oceanic and atmospheric features. In Figure 2.4 and Figure 2.5, these images can be seen.
Figure 2.4 shows three periods of dust outbreaks from the Sahara. The first Saharan dust outbreak (during the experiment) occurred in the middle of March 2015. From March 9 to March 16, optically dense dust plumes can be seen over the North–East Atlantic, partially covering the dark surface of the ocean. The map section shows parts of the Atlantic and western parts of Africa instead of Cyprus, due to the fact, that the dust particles were best seen over this area. Only a low concentration of dust particles reached Cyprus and mixing with other particles occurred. Therefore, no dust plumes were visible from space over the Mediterranean Sea at that time. One week later, Saharan desert dust was transported to the north and northeast and was visible from space over the Mediterranean Sea from March 23 to March 28. Another dust outbreak towards the Mediterranean Sea took place in the beginning of April 2015. A dense dust plume can be seen over the Mediterranean Sea on April 6 and 7, reaching Cyprus on April 7, 2015.

In Figure 2.5, two periods of dust outbreaks from the Middle East are shown. In the beginning of March, a dust outbreak from the Arabian Peninsula towards the west and northwest occurred. Dust was visible from space from March 6 to March 8 over the Mediterranean and Red Sea. A heavy dust storm was detected in April 2015, visible over the Arabian and Red Sea for almost 2 weeks. From April 2 to April 14, 2015, huge parts of the sea were covered by dense dust plumes, spreading out in almost all directions.

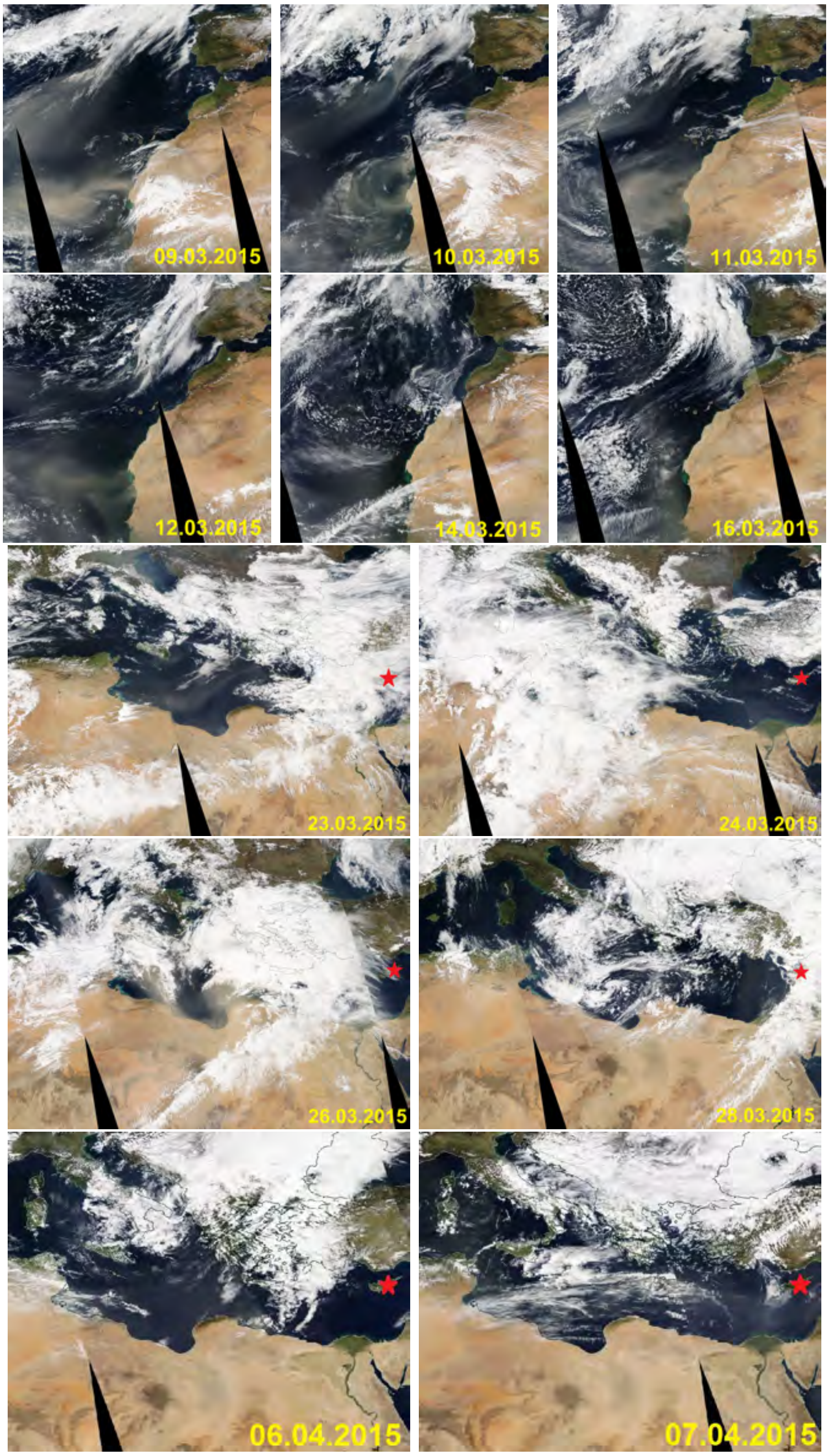

Figure 2.4: Saharan Dust Outbreaks. First and second row: dust outbreak in the central Sahara, visible over the North–East Atlantic (09.03.–16.03.2015), third and fourth row: dust outbreak from the central Sahara towards the Mediterranean Sea (23.03.–28.03.2015), fifth row: dust storm over North Africa, visible over the Mediterranean Sea (06./07.04.2015), red star: Cyprus (https://worldview.earthdata.nasa.gov)

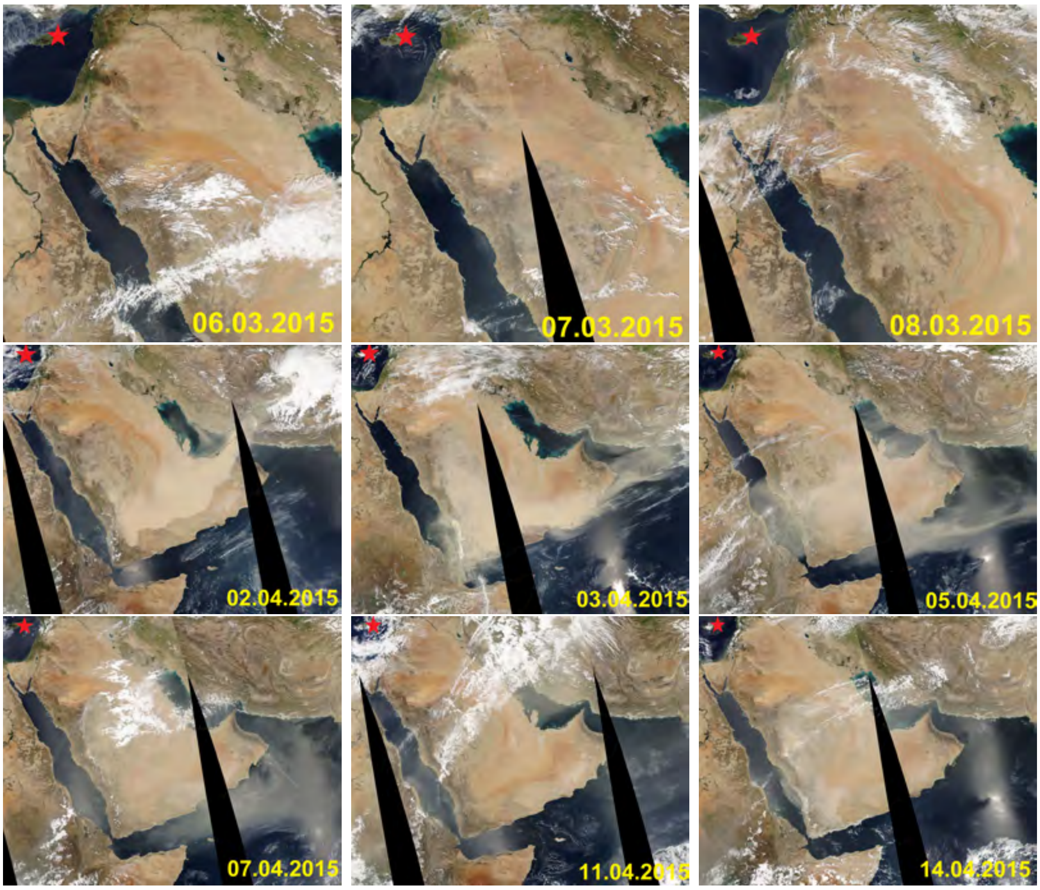

Figure 2.5: Middle East Dust Outbreaks. First row: dust storm over the Arabian Peninsula, visible over the Mediterranean and Red Sea (06.03.–08.03.2015), second and third row: dust outbreak towards the Arabian and Red Sea (02.04.–14.04.2015), red star: Cyprus (https://worldview.earthdata.nasa.gov)

2.3 Previous Aerosol Research

For the region of Cyprus only a few studies regarding aerosol conditions are available. As seen in the preceding section, several long–term studies of dust outbreaks have been published, among them studies of dust outbreaks towards the Mediterranean (e.g. Amiridis et al. 2005; Papayannis et al. 2009). The main focus in these studies was on Saharan dust outbreaks. The first lidar–based long–term study for the eastern Mediterranean was presented by Nisantzi et al. (2015). It was based on lidar and sun/sky photometer observations at Limassol, Cyprus from 2010 to 2013 and included Saharan as well as Middle East desert dust outbreaks. During four years of measurements 32 Saharan dust cases and 17 Middle East dust cases occurred. The goal of the data analysis was to compare the lidar ratios of dust from the two different source regions.

Table 2.1: Desert dust layer statistics for 49 outbreaks (2010–2013): AERONET Ångström exponent (440–870 nm) and Fine–mode fraction (ratio of 500 nm Fine–mode AOT to AOT) for the tropospheric vertical column (T), and lidar–derived 532 nm Dust AOT for the free troposphere (FT), Dust fraction DF, the dust–layer mean particle linear Depolarization ratio (532 nm), the Backscatter fraction D_β, and the different Lidar ratios (for Middle East, M. E., and Saharan dust). Mean value and standard deviation (SD) are given together with the range of observed values (from minimum to maximum value) [adapted from *Nisantzi et al.*, 2015].

Parameter	Mean	SD	Min	Max
Ångström exponent (T)	0.75	0.42	0.04	1.63
Fine-mode fraction (T)	0.44	0.13	0.18	0.68
Dust AOT (FT)	0.20	0.20	0.04	1.15
Dust AOT fraction, DF (FT)	0.64	0.21	0.18	0.99
Depolarization ratio (FT)	0.24	0.04	0.17	0.35
Backscatt. fraction, D_β (FT)	0.62	0.22	0.19	0.99
Lidar ratio (M.E.), $D_\beta > 0.8$	44	1	43	46
Lidar ratio (M.E.)	41	4	33	48
Lidar ratio (Sah.), $D_\beta > 0.8$	56	6	47	65
Lidar ratio (Sah.)	53	6	43	65

In Table 2.1, values for the optical properties of the observed dust layers are listed. Mean values for the dust lidar ratios were calculated separately for a huge amount of dust within the aerosol layer ($D_\beta > 0.8$) and when considering the full data sets. By whatever means, obvious differences between the Saharan dust lidar ratio and the Middle East dust lidar ratio were found. Furthermore, Nisantzi et al. (2015) remarked the difficulty in identifying the aerosol optical properties due to complex aerosol mixtures of desert dust, marine particles, fire smoke and anthropogenic haze. In contrast to this study where measurements with a polarization–lidar and a sun/sky photometer were combined to calculate the aerosol optical properties, the presented study is based on measurements with a multiwavelength–Raman–polarization lidar with the advantage of the direct and independent derivation of the backscatter and extinction coefficient. These measurements will be introduced in the next chapter.

Chapter 3

BACCHUS–Cyprus campaign

In this chapter, the BACCHUS–Cyprus campaign including the measurement location and instrumentation and the multiwavelength–Raman–polarization lidar Polly^{XT} will be introduced.

3.1 Overview

Figure 3.1: Overview of the BACCHUS–Cyprus campaign. Measurements were performed at Nicosia, Agia Marina and Limassol. [Figure provided by TROPOS]

BACCHUS (Impact of Biogenic versus Anthropogenic emissions on Clouds and Climate: towards a Holistic UnderStanding) is an European collaborative project under the lead of the Swiss Federal Institute of Technology in Zurich. From 2013 to 2017, 21 research institutions from the European Union, Switzerland, Norway and Israel work closely together with the goal of a better understanding of key processes in aerosol–cloud interacting (http://bacchus env.eu/ 2017). Since 2013 several campaigns took place, one of them in Cyprus in spring 2015.

During the BACCHUS–Cyprus campaign, observations with different instruments were performed at Nicosia, Agia Marina and Limassol. Figure 3.1 shows an overview of the measurement locations. The Leibniz Institute for Tropospheric Research (TROPOS) Leipzig was involved in this campaign, performing measurements at Nicosia ($35\,^\circ\,10'\,\mathrm{N}, 33\,^\circ\,21'\,\mathrm{E}$). Nicosia is located in the center of Cyprus, local time is UTC+2. On the roof of the Cyprus Institute at Nicosia different instruments were installed, as can be seen in Figure 3.2.

Besides the multiwavelength–Raman–polarization lidar Polly$^{\mathrm{XT}}$, a sun/sky/lunar photometer and a Wind Doppler Lidar were installed at 185 m above sea level.

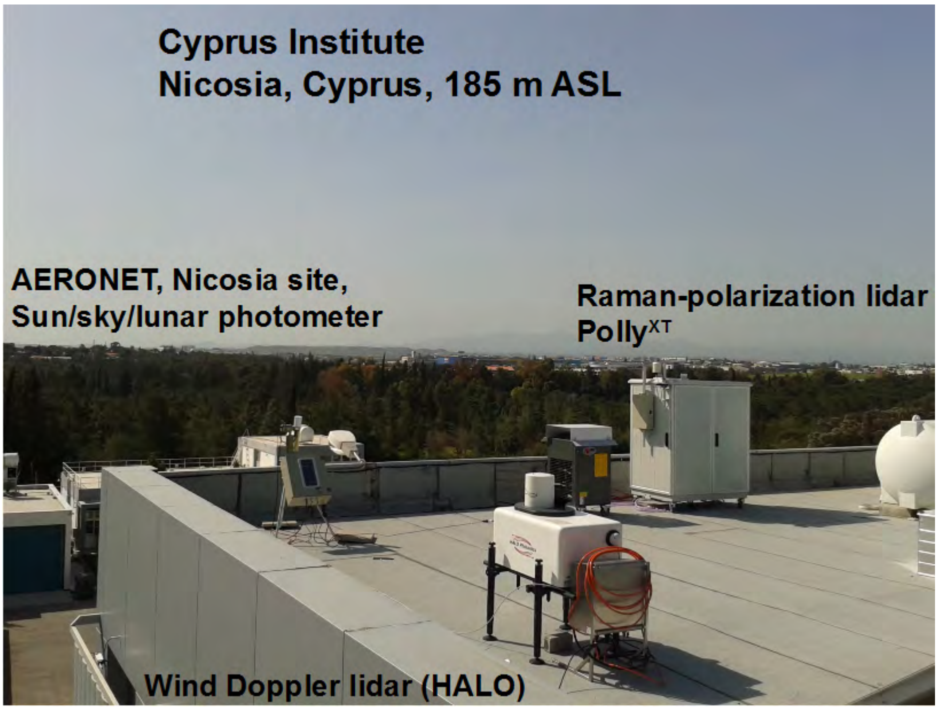

Figure 3.2: Installation of instruments at Nicosia during the BACCHUS–Cyprus campaign [picture provided by TROPOS].

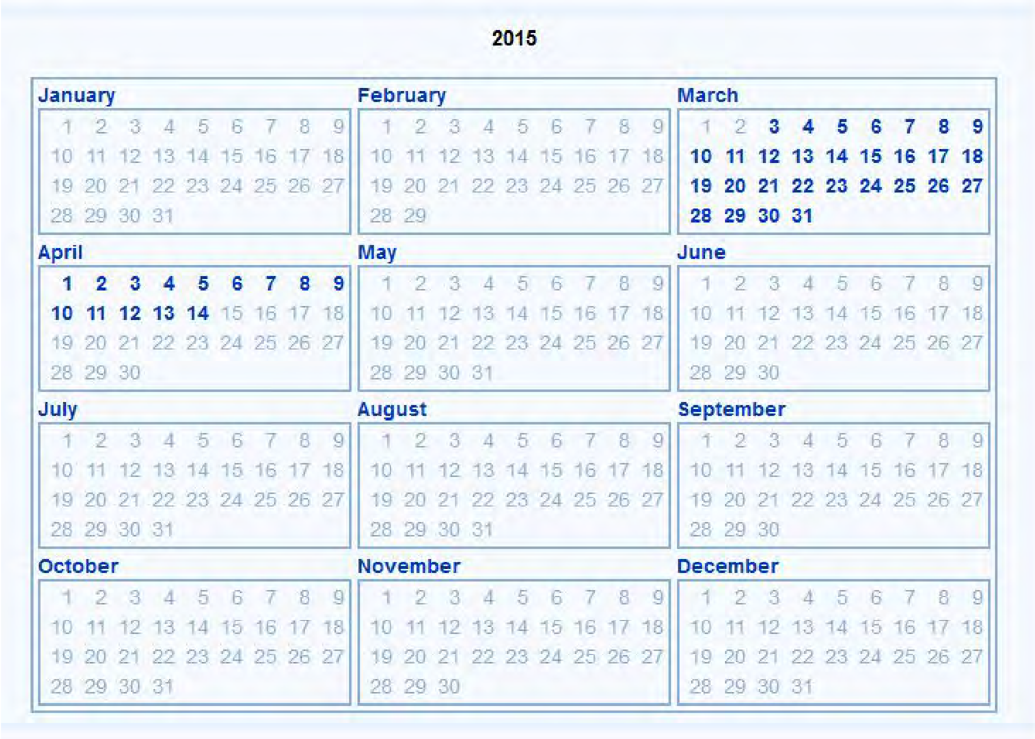

Figure 3.3: Measurement Calendar of observations with Polly^{XT} at Nicosia during the BACCHUS–Cyprus campaign (http://polly.tropos.de, Cyprus site).

These instruments performed fully automated observations.

Figure 3.3 shows the calendar for the Polly^{XT} measurements at Nicosia during the BACCHUS–Cyprus campaign. Days of observation are printed in bold type. Measurements took place from March 3, 2015 till April 14, 2015. The measurement calendar is available on the webpage polly.tropos.de (Cyprus site). Height–time displays of the range–corrected signal are accessible for each observation day.

Now we will have a look at Polly^{XT}, the multiwavelength–Raman–polarization lidar that was used during the BACCHUS–Cyprus campaign.

3.2 Polly^{XT}

Polly is a portable lidar that was developed at TROPOS in 2003. Since then, the lidar system was continuously improved during various field campaigns and with gained experience from EARLINET (European Aerosol Research Lidar Network)(Engelmann et al. 2016).

The measurement data is collected within a network called PollyNet (http://polly.tropos.de) to ensure data backup and an international transfer of knowledge. The first Polly, that was developed in 2003, was a single–wavelength Raman lidar. Polly$^{\mathrm{XT}}$ is a multiwavelength–Raman–polarization lidar with eXTended capabilities (Engelmann et al. 2016). During worlwide field campaigns a huge data set was achieved using Polly$^{\mathrm{XT}}$.
The most recent version of Polly$^{\mathrm{XT}}$, called Polly$^{\mathrm{XT}}$_ OCEANET, is a 3+2+2+2+1 lidar, which means that the backscatter coefficient is determined at three wavelengths and the extinction coefficient at two wavelenghts, the instrument has two depolarization–sensitive channels, two receiver units for the near range and an additional water–vapor channel (Engelmann et al. 2016).

The version of Polly$^{\mathrm{XT}}$ that was used during the BACCHUS–Cyprus campaign was developed following the OCEANET design and is called Polly$^{\mathrm{XT}}$_ NOA since it is now put into service at the National Observatory of Athens (NOA, Greece).

The optical setup is shown in Figure3.4. The laser of the lidar (E1) emits light pulses at 1064 nm with a repetition frequency of 20 Hz. After the alignment of the laser beam through the external second and third harmonic generators (E2), laser pulses with energies of 180 mJ at 1064 nm, 110 mJ at 532 nm, and 60 mJ at 355 nm are emitted. An external power meter (E2a) is used for later quality control. By the use of a waveplate and a Brewster–cut Glan–laser polarizer (E3), the purity of the linear polarization of the pulses at all wavelengths is warranted. The light is redirected upwards by means of two dichroic mirrors. The additional shutter (E4) prohibits the emission of laser light during airplane overflights. Before the light is emitted into the atmosphere, the beam is expanded (E5).

A Newtonian telescope (R2) is included in the far–range receiver unit of all Polly$^{\mathrm{XT}}$–systems. In front of the pinhole (R3) a device for the absolute calibration of the depolarization measurements is mounted. Afterwards, the received light is collimated by a lens pair and separated by wavelength by dichroic beam splitters. A camera (CAM) monitors the stability of the laser–beam overlap with the receiving telescope.

A second telescope (R1) creates the requirements for the near–range profiling. The field of view of the near–range receiver is 2.2 mrad and the region of complete overlap is at about 120 m. Before the signals are detected at 532 and 607 nm, the light passes a dichroic beam splitter and neutral–density and interference filters. A more detailed description of Polly$^{\mathrm{XT}}$_ OCEANET is presented in Engelmann et al. (2016).

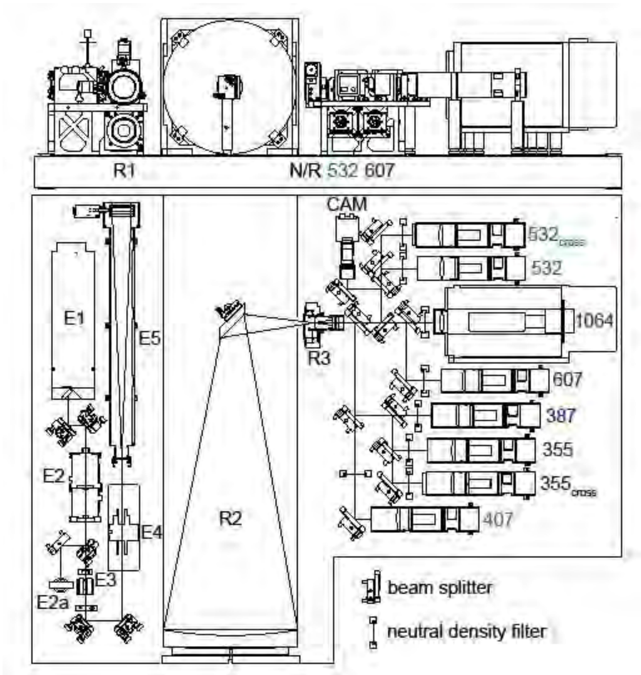

Figure 3.4: The optical setup of Polly^{XT}- OCEANET, top view (upper part) and front view (lower part). The emitter and receiver unit are indicated by "E" and "R" respectively, the near–range receiver unit by "N/R". E1: laser head, E2: second and third harmonic generators, E2a: external power meter, E3: Brewster–cut Glan–Laser polarizer, E4: shutter for airplane overflights, E5: beam expander, R1: near–range telescope, R2: Newtonian telescope (far–range), R3: pinhole, CAM: camera [adapted from *Engelmann et al.*, 2016].

The optical setup was mounted on a carbon–fiber optical board, which is tilted by 5 ° to avoid specular reflections from horizontally aligned ice crystals.

With Polly^{XT}, observations up to a height of approximately 40 km are possible with a height resolution of 7.5 m. Profiles are averaged over a time period of 30 s. In case of rain events, the measurements are automatically interrupted.

Chapter 4

Methodology

In this chapter, the lidar principle and the gain of the aerosol optical properties will be described. The lidar equation as well as the determination of the backscatter and extinction coefficient with two different methods (Klett–Method and Raman–Lidar–Method) will be introduced. Calculations of the lidar ratio, the Ångström exponent and the particle linear depolarization ratio, important key factors for aerosol characterization, will be shown.

4.1 Lidar

The acronym LIDAR means 'light detection and ranging'. The laser transmitter of a lidar generates a laser pulse which is sent into the atmosphere. The backscattered light is detected and gives information about the air masses above the instrument. The range R of the scattering height level can be calculated with the velocity of light c and the time t between pulse emission and signal detection:

$$R = \frac{ct}{2} \tag{4.1}$$

4.1.1 Lidar equation

The gained signal can be described by the lidar equation for elastic backscattering (Wandinger 2005):

$$\begin{aligned} P(R,\lambda) = {} & \underbrace{P_0(\lambda)\frac{c\tau(\lambda)}{2}\eta(\lambda)A_{Tel}}_{1}\underbrace{\frac{O(R)}{R^2}}_{2} \\ & \times \underbrace{[\beta_{\text{mol}}(R,\lambda)+\beta_{\text{par}}(R,\lambda)]}_{3}\underbrace{\exp\left\{-2\int_0^R[\alpha_{\text{mol}}(r,\lambda)+\alpha_{\text{par}}(r,\lambda)]\,\mathrm{d}r\right\}}_{4}. \end{aligned} \tag{4.2}$$

On the left side of this equation is the detected power $P(R,\lambda)$ and on the right side we find four terms that will now be explained.

The first term on the right shows the system factor which includes the instrument specific properties, that are the emitted pulse power $P_0(\lambda)$ at wavelength λ, the temporal pulse length $\tau(\lambda)$, the velocity of light c, the system efficiency $\eta(\lambda)$ and the area of the receiver telescope A_{Tel}.

The second term denotes the range–dependent geometrical measurement properties and includes the overlap function $O(R)$ of the laser beam and receiver field of view. $O(R)$ is zero at the measurement instrument and one if the laser beam can be completely depicted by the detector. This term also shows that the power signal decreases with the square of the distance R.

The third term is the backscatter coefficient $\beta(R,\lambda)$. It describes the amount of radiation that is scattered in backward direction under an angle of 180 °. The laser light can be backscattered by molecules (mol) and particles (par).

The last term of the lidar equation is the transmission term. It includes the extinction coefficient $\alpha(R,\lambda)$ that describes the amount of radiation that is absorbed and scattered by molecules (mol) and particles (par). The extinction coefficient is integrated over range from $R = 0$ at the lidar to the height R. The two–way photon travel path from the lidar and back is denoted by the factor 2 in this term.

As already mentioned, the received signal intensity decreases with increasing distance. The range–corrected signal $P(R,\lambda)R^2$ can be obtained by multiplying the received signal with R^2:

$$\begin{aligned} P(R,\lambda)R^2 = {} & P_0(\lambda)\frac{c\tau(\lambda)}{2}\eta(\lambda)A_{Tel}O(R) \\ & \times [\beta_{\text{mol}}(R,\lambda)+\beta_{\text{par}}(R,\lambda)]\exp\left\{-2\int_0^R[\alpha_{\text{mol}}(r,\lambda)+\alpha_{\text{par}}(r,\lambda)]\,\mathrm{d}r\right\}. \end{aligned} \tag{4.3}$$

The backscatter and extinction coefficient are important factors for the characterization of the scattering particles. To derive these quantities, two methods can be applied, the Klett–Method and the Raman–Lidar–Method. These methods will now be explained seperately.

4.1.2 Klett–Method

In case of the Klett–Method, a reference height R_0 is introduced and for this height the backscatter coefficient has to be assumed. A reference height is chosen where particle scattering is small compared to Rayleigh scattering which is known. We get the following equation for the particle backscatter coefficient $\beta_{par}(R, \lambda_0)$ (Klett 1981):

$$\beta_{par}(R, \lambda_0) = \frac{A(R_0, R, \lambda_0)}{B(R_0, \lambda_0) - 2LR_{par}(\lambda_0) \int_{R_0}^{R} A(R_0, r, \lambda_0) dr} - \beta_{mol}(R, \lambda_0) \tag{4.4}$$

with

$$A(R_0, x, \lambda_0) = x^2 P(x, \lambda_0) \exp\left[-2(LR_{par}(\lambda_0) - LR_{mol}) \int_{R_0}^{x} \beta_{mol}(r, \lambda_0) dr\right] \tag{4.5}$$

and

$$B(R_0, \lambda_0) = \frac{{R_0}^2 P(R_0, \lambda_0)}{\beta_{par}(R_0, \lambda_0) + \beta_{mol}(R_0, \lambda_0)} \tag{4.6}$$

The extinction coefficient $\alpha_{par}(R, \lambda_0)$ can be calculated with the particle lidar ratio $LR_{par}(R, \lambda_0)$:

$$LR_{par}(R, \lambda_0) = \frac{\alpha_{par}(R, \lambda_0)}{\beta_{par}(R, \lambda_0)} \tag{4.7}$$

The particle lidar ratio has to be assumed. Characteristic values for different aerosol types in the atmosphere are chosen.

4.1.3 Raman–Lidar–Method

The Raman–Lidar–Method provides an independent determination of the particle backscatter and extinction coefficient.

In addition to the elastically backscattered lidar signal, the inelastically backscattered lidar signal is detected. In case of inelastic scattering, molecules change their rotational and/or vibrational state. This is called Raman process and leads to a frequency shift of the backscattered light. Therefore a wavelength different from the emitted wavelength is detected, the Raman wavelength λ_{Ra}. It is well known for oxygen and nitrogen.

The detected power at the Raman wavelength can be described as follows (Wandinger 2005):

$$\begin{aligned} P(R,\lambda_{Ra}) = & \underbrace{P_0(\lambda)\frac{c\tau(\lambda_{Ra})}{2}\eta(\lambda_{Ra})A_{Tel}}_{1}\underbrace{\frac{O(R)}{R^2}}_{2} \\ & \times \underbrace{\beta_{Ra}(R,\lambda_{Ra})}_{3}\underbrace{\exp\left\{-\int_0^R [\alpha(r,\lambda)+\alpha(r,\lambda_{Ra})]\,\mathrm{d}r\right\}}_{4}. \end{aligned} \tag{4.8}$$

As in equation(4.2) we find the detected power on the left and four terms on the right side of the equation. The system factor (1) now shows a Raman wavelength dependent temporal pulse length $\tau(\lambda_{Ra})$ and system efficiency $\eta(\lambda_{Ra})$. Again, the geometry factor (2) appears as in equation (4.2), including the overlap function O(R) of the laser beam and receiver field of view. The backscatter coefficient (3) is measured at the Raman wavelength and the transmission term (4) now consists of an elastic part $\alpha(r,\lambda)$ for the way up to the scattering particle and an inelastic part $\alpha(r,\lambda_{Ra})$ for the way back to the instrument. With a Raman–lidar, profiles of the backscatter and extinction coefficient can be derived directly and independently by measurements of the elastic signal $P(R,\lambda_0)$ and the inelastic Raman signal $P(R,\lambda_{Ra})$.
The backscatter coefficient can be determined as follows (Ansmann et al. 1992):

$$\begin{aligned} \beta_{par}(R,\lambda_0) = & [\beta_{par}(R_0,\lambda_0)+\beta_{mol}(R_0,\lambda_0)] \\ & \times \frac{P(R_0,\lambda_{Ra})P(R,\lambda_0)N_{Ra}(R)}{P(R_0,\lambda_0)R(R,\lambda_{Ra})N_{Ra}(R_0)} \\ & \times \frac{\exp\left\{-2\int_{R_0}^R [\alpha_{mol}(r,\lambda_{Ra})+\alpha_{par}(r,\lambda_{Ra})]\,\mathrm{d}r\right\}}{\exp\left\{-2\int_{R_0}^R [\alpha_{mol}(r,\lambda_0)+\alpha_{par}(r,\lambda_0)]\,\mathrm{d}r\right\}} \\ & - \beta_{mol}(R,\lambda_0). \end{aligned} \tag{4.9}$$

A reference height R_0 is chosen where particle scattering is small compared to Rayleigh scattering. For this height the backscatter coefficient has to be assumed. N_{Ra} is the molecular particle number density of the regarded gas.

For oxygen and nitrogen this parameter can be easily calculated with temperature and pressure profiles derived by soundings or atmospheric model data.

The extinction coefficient is derived as follows (Ansmann et al. 1990):

$$\alpha_{par}(R,\lambda_0) = \frac{\frac{d}{dR}\left[\ln\frac{N_{Ra}(R)}{R^2 P_{Ra}(R)}\right] - \alpha_{mol}(R,\lambda_0) - \alpha_{mol}(R,\lambda_{Ra})}{1+(\frac{\lambda_0}{\lambda_{Ra}})^{\mathring{a}_\alpha}} \tag{4.10}$$

with the extinction–related Ångström exponent $\mathring{a}_\alpha$, that describes the dependency of the extinction coefficient on the wavelength.

With the backscatter and extinction coefficient several intensive parameters can be calculated: the particle lidar ratio $LR_{par}(R,\lambda)$, the Ångström exponent $\mathring{a}_{\alpha/\beta}(R)$ and the particle linear depolarization ratio $\delta_{par}(R,\lambda)$. These quantities will be described in the next section.

4.2 Aerosol optical properties

The relationship between extinction and backscatter coefficient is expressed by the lidar ratio $LR_{par}(R,\lambda)$:

$$LR_{par}(R,\lambda) = \frac{\alpha_{par}(R,\lambda)}{\beta_{par}(R,\lambda)} \tag{4.11}$$

It depends on the size distribution, shape and chemical properties of the scattering particles and is therefore an important key factor for aerosol characterization.
The Ångström exponent $\mathring{a}_{\alpha/\beta}(R)$ can be either calculated with the extinction (α_{par}) or backscatter coefficient (β_{par}), measured at two different wavelengths λ_0 and λ_1:

$$\mathring{a}_\alpha(R) = -\frac{\ln(\frac{\alpha_{par}(\lambda_1)}{\alpha_{par}(\lambda_0)})}{\ln(\frac{\lambda_1}{\lambda_0})} \tag{4.12}$$

$$\mathring{a}_\beta(R) = -\frac{\ln(\frac{\beta_{par}(\lambda_1)}{\beta_{par}(\lambda_0)})}{\ln(\frac{\lambda_1}{\lambda_0})} \tag{4.13}$$

The Ångström exponent is inversely proportional to the particle size, that means the smaller the particles, the larger the Ångström exponent.

The state of polarization of the emitted laser light can change during the scattering process. This depends on the geometrical properties of the scattering particles. With a polarization–lidar the volume depolarization ratio can be derived by measuring the parallel and cross polarized signal component of the backscattered light. The emitted laser light is linear polarized.
If the light is depolarized by non–spherical scattering particles, such as ice crystals or dust particles, a significant cross–polarized signal component $P(R)_{\perp}^{\mathrm{Tel}}$ can be noticed in the lidar telescope (Seifert 2010; Sassen 2005):

$$P(R)_{\perp}^{\mathrm{Tel}} = P_{0,\parallel} C \frac{O(R)}{R^2} \beta_{\perp}(R) \exp\left[-\int_0^R \alpha_{\perp}(r) + \alpha_{\parallel}(r) \mathrm{d}r\right]. \tag{4.14}$$

The parallel–polarized signal component $P(R)_{\parallel}^{\mathrm{Tel}}$ is rather weak in the case of non–spherical scattering particles:

$$P(R)_{\parallel}^{\mathrm{Tel}} = P_{0,\parallel} C \frac{O(R)}{R^2} \beta_{\parallel}(R) \exp\left[-2\int_0^R \alpha_{\parallel}(r) \mathrm{d}r\right]. \tag{4.15}$$

The volume depolarization ratio $\delta^{\mathrm{vol}}(R)$ is the ratio of the cross–polarized to parallel–polarized signal and can be calculated as follows (Sassen 2005):

$$\delta^{\mathrm{vol}}(R) = \frac{P_{\perp}^{\mathrm{Tel}}(R)}{P_{\parallel}^{\mathrm{Tel}}(R)} = \frac{\beta_{\perp}(R)}{\beta_{\parallel}(R)} = \frac{\beta_{\perp}^{\mathrm{par}}(R) + \beta_{\perp}^{\mathrm{mol}}(R)}{\beta_{\parallel}^{\mathrm{par}}(R) + \beta_{\parallel}^{\mathrm{mol}}(R)}, \tag{4.16}$$

assuming the system and geometry factors to be equal and $\alpha_{\parallel} = \alpha_{\perp}$. The volume depolarization ratio is now a function of the cross– and parallel–polarized backscatter coefficient $\beta_{\perp}(R)$ and $\beta_{\parallel}(R)$. It can be separated into a molecular depolarization ratio $\delta_{mol}(R)$

$$\delta_{mol}(R) = \frac{\beta_{\perp}^{\mathrm{mol}}(R)}{\beta_{\parallel}^{\mathrm{mol}}(R)} \tag{4.17}$$

and a particle linear depolarization ratio $\delta_{par}(R)$

$$\delta_{par}(R) = \frac{\beta_{\perp}^{\mathrm{par}}(R)}{\beta_{\parallel}^{\mathrm{par}}(R)}. \tag{4.18}$$

The separation is a difficult task leading to the following equation for the particle linear depolarization ratio (Tesche et al. 2009):

$$\delta_{par}(R) = \frac{\beta_{mol}(R)(\delta_{vol}(R) - \delta_{mol}(R)) + \beta_{par}(R)\delta_{vol}(R)(1 + \delta_{mol}(R))}{\beta_{mol}(R)(\delta_{mol}(R) - \delta_{vol}(R)) + \beta_{par}(R)(1 + \delta_{mol}(R))}. \tag{4.19}$$

With the particle linear depolarization ratio, information about the sphericity of the scattering particles can be obtained. Backscattering by spherical particles produces only very low depolarization, hence the particle linear depolarization ratio is zero or almost zero ($\delta_{par}(R) \sim 0$). In the case of backscattering by non–spherical particles, the emitted light is strongly depolarized during the backscattering process ($\delta_{par}(R) > 0$).

Equation (4.16) is only valid under ideal conditions. Most lidar instruments show unequal efficiencies for all the optical elements that reflect and transmit photons of the parallel– and cross–polarized light on the way from the telescope (Tel) to the detector (Det). To calculate the depolarization ratio correctly, this has to be taken into account. For the detected cross–polarized signal component $P(R)_{\perp}^{\mathrm{Det}}$ and the detected parallel–polarized signal component $P(R)_{\parallel}^{\mathrm{Det}}$ we get:

$$P(R)_{\perp}^{\mathrm{Det}} = \eta_{\perp}^{\mathrm{Det}} P(R)_{\perp}^{\mathrm{Tel}} \tag{4.20}$$

$$P(R)_{\parallel}^{\mathrm{Det}} = \eta_{\parallel}^{\mathrm{Det}} P(R)_{\parallel}^{\mathrm{Tel}}, \tag{4.21}$$

whereby $\eta_{\perp}^{\mathrm{Det}}$ and $\eta_{\parallel}^{\mathrm{Det}}$ describe the signal loss between telescope and detector for the cross–polarized and parallel–polarized signal component, respectively.
Since $P(R)_{\perp}^{\mathrm{Det}}$ and $P(R)_{\parallel}^{\mathrm{Det}}$ are measured, the equation (4.16) for the volume depolarization ratio is altered to:

$$\delta^{\mathrm{vol}}(R) = \frac{P_{\perp}^{\mathrm{Tel}}(R)}{P_{\parallel}^{\mathrm{Tel}}(R)} = \frac{\eta_{\parallel}^{\mathrm{Det}} P(R)_{\perp}^{\mathrm{Det}}}{\eta_{\perp}^{\mathrm{Det}} P(R)_{\parallel}^{\mathrm{Det}}} = D\frac{P(R)_{\perp}^{\mathrm{Det}}}{P(R)_{\parallel}^{\mathrm{Det}}}. \tag{4.22}$$

D is a calibration factor and varies from instrument to instrument. To determine D, the $\pm 45°$–calibration is used, introduced by Freudenthaler et al. (2009).

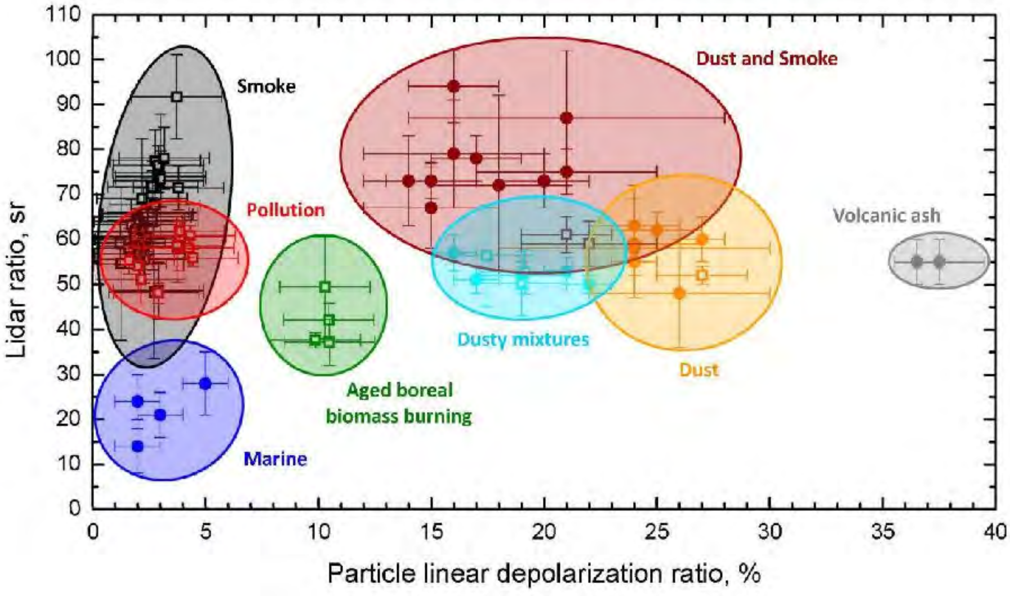

Figure 4.1: Lidar ratio and particle linear depolarization ratio at 355 nm (TROPOS (squares) and University of Munich (dots), measurements at Cape Verde, Leipzig, Munich, in the Amazon Basin and over the North Atlantic) [adapted from *Illingworth et al.*, 2015]

For different aerosol types characteristic values of the lidar ratio, the Ångström exponent and the particle linear depolarization ratio have been found. An overview of different aerosol types that have been observed during several campaigns is shown in Figure 4.1.
Values of the lidar ratio and the particle linear depolarization ratio at 355 nm for different aerosol types and mixtures are plotted against each other (Illingworth et al. 2015).

Ground–based observations with Raman–polarization lidars have been performed at the Cape Verde Islands, Leipzig, Munich, the Amazon Basin and over the North Atlantic (Groß et al. 2012; Groß et al. 2011; Baars et al. 2011; Kanitz 2012). It is obvious that the particle linear depolarization ratio shows the largest differences for the different aerosol types. The spread ranges from low values of 2 to 5 % for marine aerosol, pollution and smoke to highest values for volcanic ash (37 %). Dust and dust mixtures are in the range between 15 and 28 %.
The lidar ratio shows its lowest values for marine aerosol (15–30 sr) and highest values for smoke and mixtures of dust and smoke (50–95 sr). All other aerosol types are in the range from 35 to 70 sr.
Only a few studies of the Ångström exponent are available. Observed values vary between 0 and 2 for marine aerosol, 0 and 1 for dust and dust mixtures and 1.5 and 2 for smoke.

Pollution has an Ångström exponent of about 1 and somewhat larger than 1 (Toledano et al. 2007). Values for pure dust of 0 to 0.3 were found by Tesche et al. (2009) and values for mixtures of dust and smoke of about 0.7 by Tesche et al. (2011).

Chapter 5

Results – Part I: Case Studies

In the following two chapters, the results of the BACCHUS–Cyprus campaign will be presented, starting with the discussion of several case studies, followed by a statistical analysis of the aerosol conditions in Cyprus during the campaign.

First, an overview of the entire BACCHUS–Cyprus campaign is given. In Figure 5.1, the time–height plots of the range–corrected signal at 1064 nm and the volume depolarization ratio at 532 nm for all lidar measurements in Nicosia in the month of March 2015 (03.03.–31.03.2015) are shown. Figure 5.2 shows the time–height plots for all lidar measurements of April 2015 (01.04.–14.04.2015). During the entire campaign, the atmosphere above Nicosia was characterized by a huge amount of aerosol particles within the planetary boundary layer (PBL) with top heights of about 2 km. High–level clouds between 6 and 11 km, mid–level clouds between 2 and 6 km and low–level clouds within the PBL were frequently detected during March 2015 (dark red in Fig. 5.1, top), whereas April was less cloudy. In the case of rainfall, the measurements were interrupted, which can be seen as dark blue vertical lines in the time–height plot of the range–corrected signal and the volume depolarization ratio. The presence of non–spherical scatterers such as mineral dust and ice crystals in high–level clouds is indicated by an increased volume depolarization ratio. Dust outbreaks from the Saharan desert and deserts in the Middle East, as introduced in Chapter 2.2, affected Cyprus several times in March and April 2015 (turquoise to yellow colors in the time–height plots of the volume depolarization ratio). It can be also seen, that dust was mixed into the planetary boundary layer in many cases. A detailed analysis of the observed aerosol layers will be presented in Chapter 6.

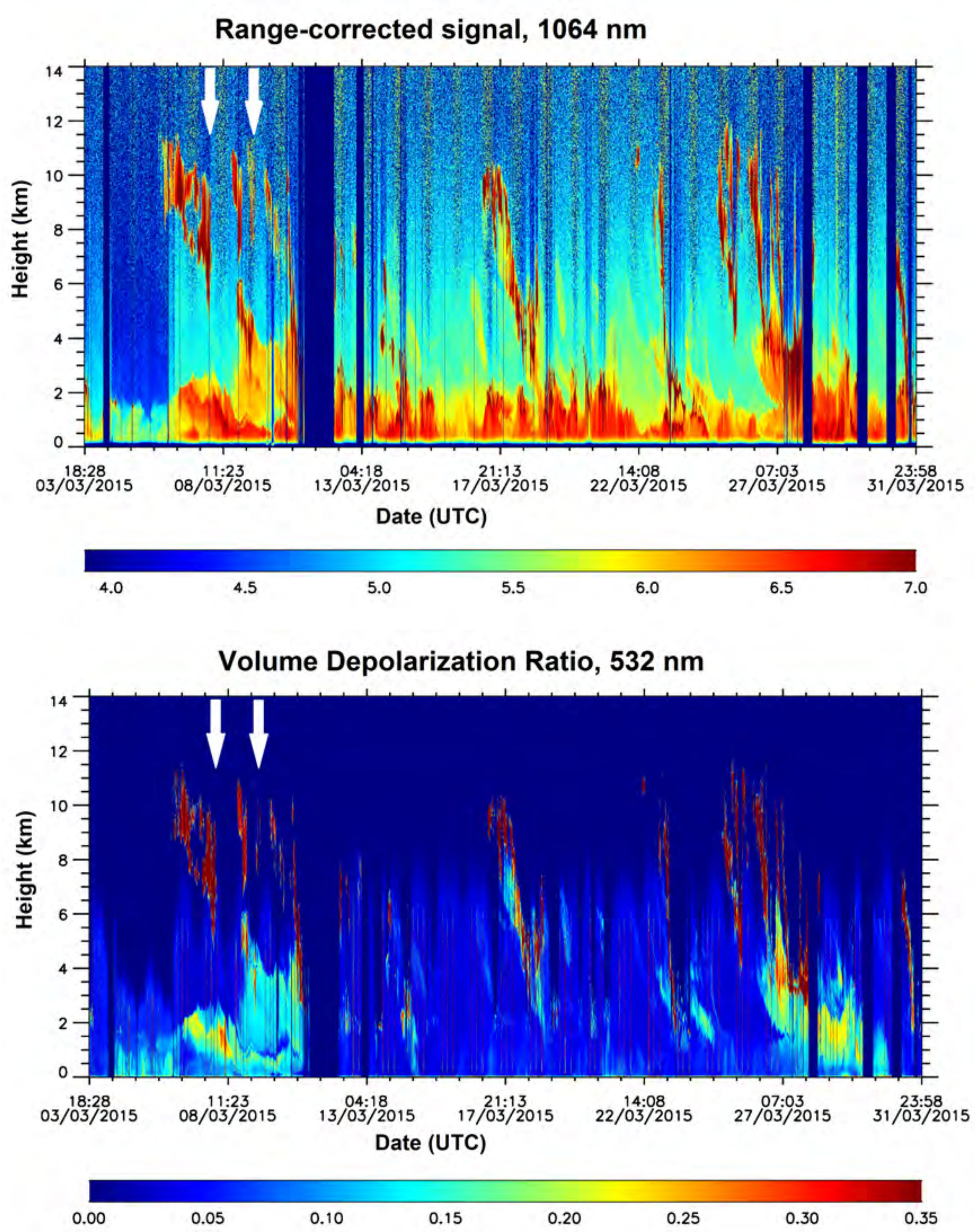

Figure 5.1: Time–height plot of the range–corrected signal at 1064 nm (top) and the 532 nm volume depolarization ratio (bottom) for March 2015 (Nicosia, Cyprus). Measurement periods for case studies are indicated by white arrows.

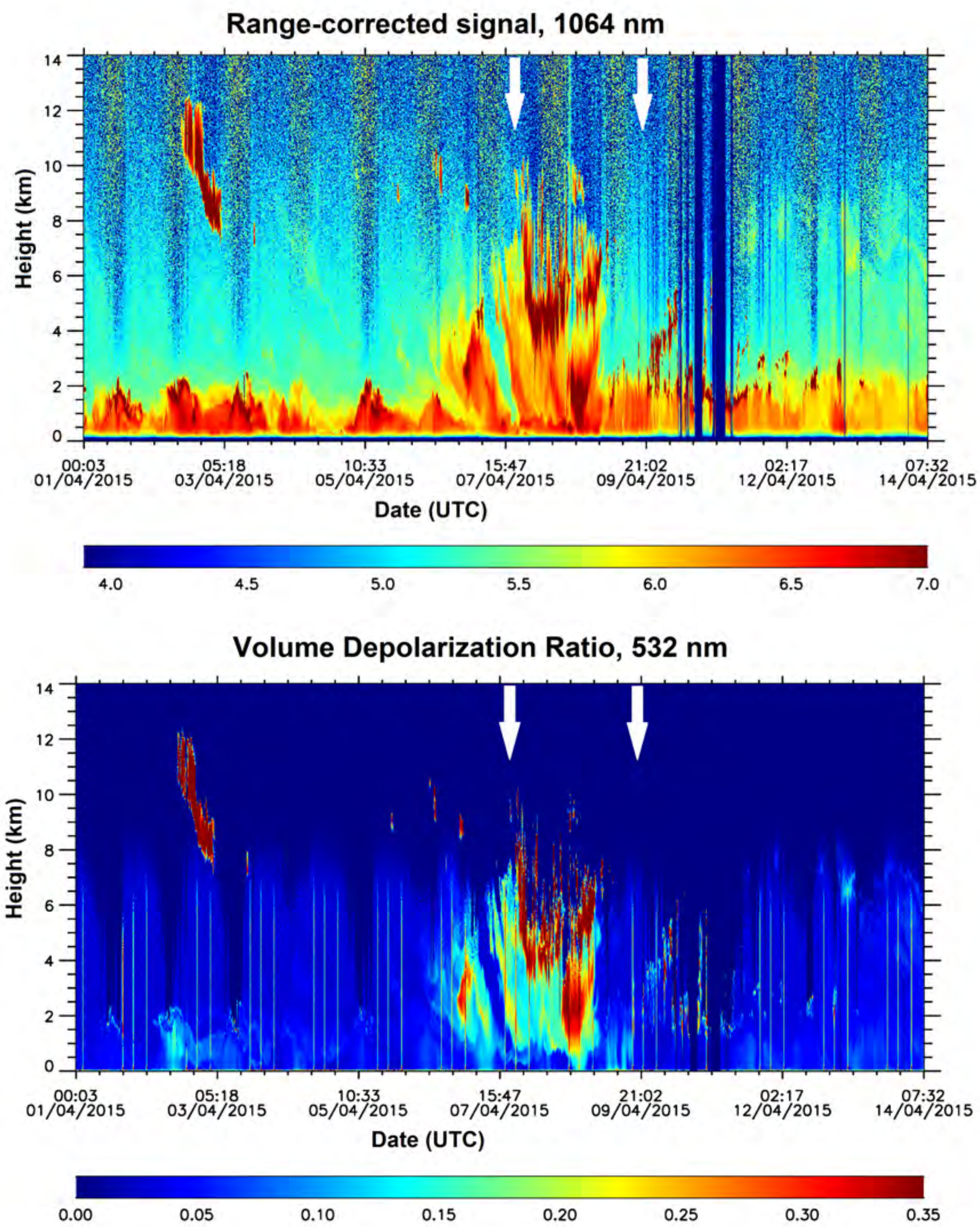

Figure 5.2: Time–height plot of the range–corrected signal at 1064 nm (top) and the 532 nm volume depolarization ratio (bottom) for April 2015 (Nicosia, Cyprus). Measurement periods for case studies are indicated by white arrows.

Four measurement periods, indicated by the white arrows in Figure 5.1 and Figure 5.2, were chosen for detailed case studies: Late evening measurements with the multiwavelength–Raman–polarization lidar Polly^{XT}_ NOA from March 7, March 9, April 7 and April 9, 2015. The observed aerosol layers are diverse and already give an overview of typical aerosol conditions in Cyprus.

Every case study follows the same strategy:
First, the time–height plot of the range–corrected signal, measured at 1064 nm with Polly^{XT}_ NOA, was analyzed with regard to aerosol layers and clouds.
To identify the origin of the observed aerosol layers, backward trajectories were used. The trajectories were calculated with the Hybrid Single–Particle Lagrangian Integrated Trajectory (HYSPLIT) model using GDAS meteorological data (Draxler and Rolph 2014). The HYSPLIT Trajectory Model is provided by the NOAA Air Resources Laboratory (ARL) via the website http://ready.arl.noaa.gov/HYSPLIT.php (2017).
For a detailed inspection of the optical properties of the aerosol layers, a period with homogeneous aerosol layers and, if possible, without clouds was chosen (indicated by the red rectangles in the time–height plots of the range–corrected signal at 1064 nm). With the Raman–Lidar–Method (see Chapter 4.1.3), the profiles of the backscatter and extinction coefficient were derived.
The lidar ratio, the Ångström exponent and the particle linear depolarization ratio were calculated. Before computing, different vertical signal smoothing lengths were applied to decrease signal noise.
The backscatter coefficients at all wavelengths were computed with a high vertical resolution of 187.5 m, as well as the particle linear depolarization ratios. The greatest smoothing length of 742.5 m was applied to the extinction–related *Ångström* exponent. The smoothing lengths for the extinction coefficients, the lidar ratios and the backscatter–related Ångström exponents vary from case to case and are in the range between 187.5 m and 742.5 m, depending on the signal–to–noise ratio of the measurements. Finally, mean values of the aerosol optical properties and their standard deviations were calculated for every aerosol layer and compared to prior studies.

5.1 Case Study: March 7, 2015

The first presented case study is from March 7, 2015. In the time–height plot of the range–corrected signal at 1064 nm (Figure 5.3), a thick aerosol layer from surface up to 2600 m and a high–level cloud layer between 5 and 10 km can be seen.

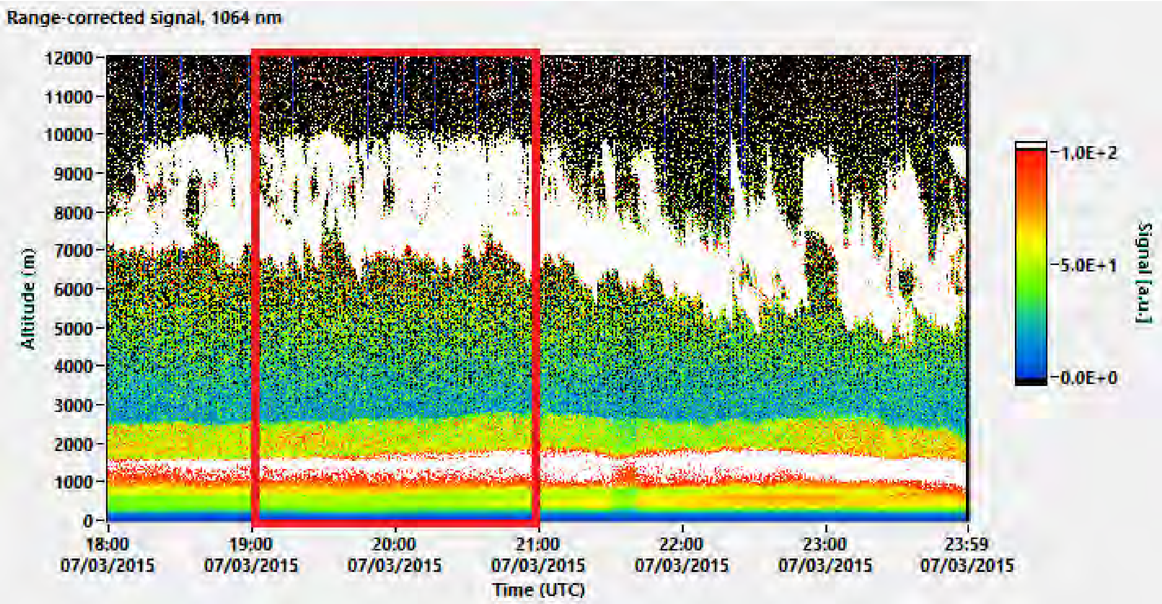

Figure 5.3: Time–height plot of the range–corrected signal at 1064 nm (07.03.2015, 18.00–00.00 UTC Nicosia, Cyprus)

Over several hours, the composition of the atmosphere over Nicosia remained almost constant, showing only weak signal changes within the 6 hours of lidar–measurements. Around 21.30 UTC, the signal weakened for a short period. Every day at that time, an automatic depolarization calibration was performed. According to Freudenthaler et al. (2009), two subsequent measurements with 90° difference were completed, achieved with a motorized filter wheel in the front of the detector.
The observed aerosol layer can be separated into 3 parts: a planetary boundary layer (PBL) up to 1100 m, an aerosol layer between 1100 and 1700 m, causing a strong signal, and an aerosol layer from 1700 to 2600 m with a weaker signal.

According to the backward trajectories (Figure 5.4) arriving at Cyprus at 20 UTC, all air masses originated from the east. The air masses of the PBL (red trajectory) were close to the ground over the Mediterranean Sea, hence mainly marine particles are expected in this layer. The air masses above originated from the Middle East (blue and green trajectory) and were close to the ground over desert areas of Syria, Jordan, the north of Saudi Arabia and the west of Iraq. There, middle east desert dust could be collected and carried to Cyprus within 2–3 days. As already discussed in Chapter 2.2, in the beginning of March 2015, a huge activity of dust storms was detected over the Arabian Peninsula. In Figure 2.5, the advection of optically dense dust plumes to Cyprus was shown (March 6 to March 8, 2015).

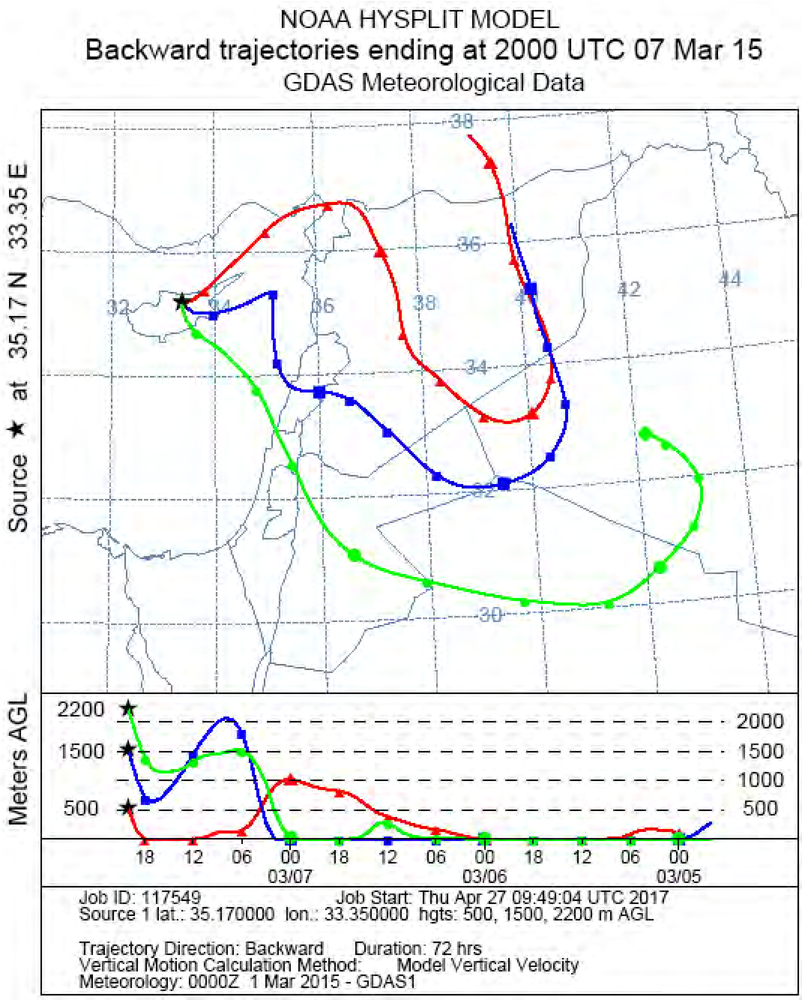

Figure 5.4: 3–day HYSPLIT backward trajectories arriving at Nicosia, Cyprus at 500 m (red), 1500 m (blue) and 2200 m (green) on March 7, 2015, 20.00 UTC (http://ready.arl.noaa.gov/HYSPLIT.php).

A high dust load in the two aerosol layers between 1.1 and 2.6 km is therefore expected. The measurement period from 19.00 to 21.00 UTC (indicated by the red rectangle in Figure 5.3) was chosen for a detailed study of the aerosol optical properties.

In Figure 5.5, profiles of the backscatter and extinction coefficient, as well as the lidar ratio, Ångström exponent and the particle linear depolarization ratio are shown. Different vertical signal smoothing lengths were used, 187.5 m for the backscatter coefficient and the particle linear depolarization ratio and 742.5 m for all other profiles. The profiles of the backscatter coefficient at the different wavelengths correlate well with each other. The near–range profile (NF 532) is in good agreement with the far–range profile at 532 nm.

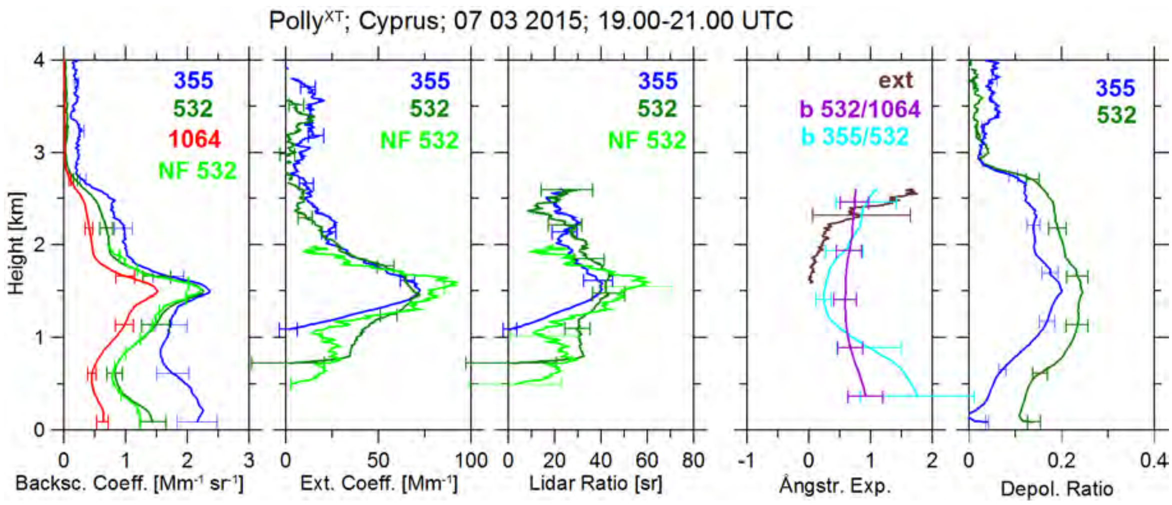

Figure 5.5: Profiles of the backscatter and extinction coefficient, lidar ratio, Ångström exponent and particle linear depolarization ratio (07.03.2015, 19.00–21.00 UTC, Nicosia, Cyprus). The vertical signal smoothing length is 187.5 m for the profiles of the backscatter coefficient and the particle linear depolarization ratio and 742.5 m for all other profiles. Colors indicate profiles for the different wavelengths.

The same applies for the profiles of the extinction coefficient. The near–range profile is clearly smaller than the 532 nm far–range profile from 0.7 to 1.3 km, which leads to an underrated calculation of the near–range lidar ratio at these heights.
Between 1.3 and 1.7 km, the near–range extinction coefficient shows significantly higher values than the profiles at 355 and 532 nm, leading to an overrated calculation of the near–range lidar ratio. The BACCHUS–Cyprus campaign was the first campaign with the new lidar Polly^{XT}_ NOA. Not all settings could have been adjusted correctly, especially the near–range channel differs from expectations in many cases. Power failures and mandatory air condition problems led to additional difficulties. Thus, the near-range extinction coefficient and lidar ratio could not be used and will be deliberately omitted in the further discussion.

The incomplete overlap between the receiver field of view and the laser beam below 1500 m is obvious in this case. At 532 nm, the extinction coefficient and lidar ratio are valid and not influenced by the overlap issue from a height of 0.8 km and at 355 nm from a height of 1.4 km in this case. As the values from the range interval of incomplete overlap could not be corrected and these values are certainly biased, they were cut out in all other case studies.
Regarding the preassigned parts of the aerosol layer up to 2.6 km, it can be noticed that the aerosol optical properties vary from part to part.

For the PBL, ranging from 100 to 1100 m, a mean lidar ratio of 32±5 sr was calculated for 532 nm, indicating that not only marine particles are present in the PBL. Mean particle linear depolarization ratios of 17±4 % (532 nm) and 8±3 % (355 nm) suggest the presence of dust in the PBL. Dust particles from the dust layer above can be transported downward by turbulent mixing processes and increase the particle linear depolarization ratio. Mean values of 1.3±0.4 and 0.8±0.1 were calculated for the backscatter–related Ångström exponents 355/532 and 532/1064.

The aerosol layer above from 1.1 to 1.7 km can be clearly classified as dust layer. The high extinction coefficient shows wavelength independence, causing a very low extinction–related Ångström exponent. This indicates the presence of mineral dust. The Ångström exponents correlate well with each other, showing mean values of 0.2±0.1 (extinction–related), 0.3±0.1 (355/532) and 0.6±0.04 (532/1064). These values are within the range of pure dust observed by Tesche et al. (2009) with the exception of the 532/1064 Ångström exponent, showing a slightly higher mean value. The particle linear depolarization ratio is almost constant within the layer with mean values of 22±2 % and 19±3 % for 532 nm and 355 nm. Mean values for the lidar ratio of 36±6 sr and 37±8 sr for 355 nm and 532 nm are comparatively small for pure dust. The above–named turbulent mixing processes may lead to an exchange of marine and dust particles within the layers and a slow increase of the lidar ratio up to typical values for dust. Between 1.4 and 1.6 km, where backscatter and extinction coefficients show their highest values, lidar ratios of about 43 sr and particle linear depolarization ratios of about 24 % (532 nm) and 20 % (355 nm) are in good agreement with findings of Nisantzi et al. (2015), regarding aerosol layers with a huge amount ($D_\beta > 0.8$) of Middle East desert dust (see also Chapter 2.3).

The aerosol layer between 1.7 and 2.6 km represents a complex dust mixture. Values of the lidar ratio and the particle linear depolarization ratio decrease from typical values for dust to mean values of 26±8 sr (355 nm) and 30±11 sr (532 nm), and 19±1% (532 nm) and 15±1% (355 nm). Ångström exponents of 0.6±0.5 (extinction–related), 0.7±0.1 (355/532) and 0.7±0.02 (532/1064) are in good agreement with the values for mixtures of dust and smoke found by Tesche et al. (2011). Backward trajectories arriving at Cyprus at 2200 m were close to the ground for two days, reaching back to Iraq, where a huge fire activity was detected in March and April 2015 (see Chapter 2.2, Figure 2.2). Typical lidar ratios for dust–smoke mixtures are in the range of 60 to 100 sr (see Fig. 4.1 in Chapter 4.2). It is expected that the presence of smoke particles within the dust layer increases the lidar ratio.

Comparatively small lidar ratios have been found by Nicolae et al. (2013) for aged smoke particles. Lidar ratios were significantly lower for smoke particles that had been in the atmosphere for 2 to 3 days before than for fresh smoke particles. It was also noticed, that the 355 nm lidar ratio showed greater values for aged smoke particles than the 532 nm lidar ratio, which shows usually greater values for most aerosol types. However, an aerosol classification in this case is difficult and the presence of aged smoke particles within the dust layer remains speculative. Most likely, Middle East desert dust is mixed with other non–absorbing particles, leading to a decreased lidar ratio.

5.2 Case Study: March 9, 2015

Lidar–measurements on March 9, 2015 were chosen for a second case study. The time–height plot of the range–corrected signal at 1064 nm (Figure 5.6) shows an aerosol layer up to 700 m, an aerosol layer between 1000 and 3800 m and cloud formation, starting around 21 UTC, between 8 and 11 km. After 22.30 UTC, the signal weakened. This may have various reasons, such as hardware problems, fog or dew.

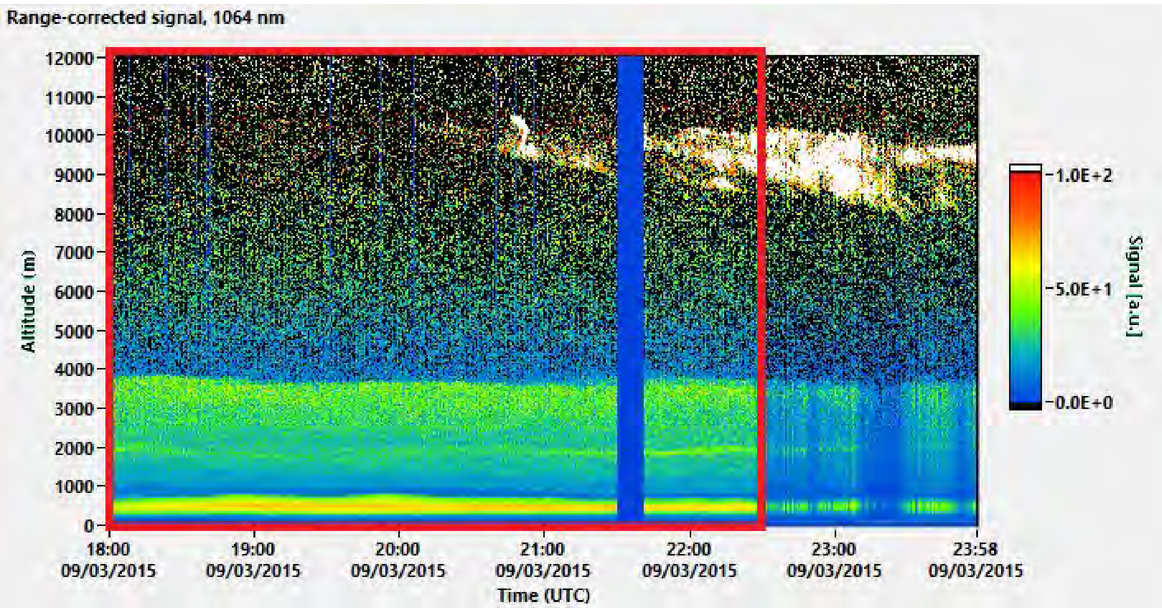

Figure 5.6: Time–height plot of the range–corrected signal at 1064 nm (09.03.2015, 18.00–00.00 UTC Nicosia, Cyprus)

Figure 5.7 shows calculated HYSPLIT backward trajectories arriving at Cyprus at 19 UTC. The air masses of the PBL (red trajectory) originated from the east and were close to the ground over the Mediterranean Sea and near the Turkish–Syrian border.

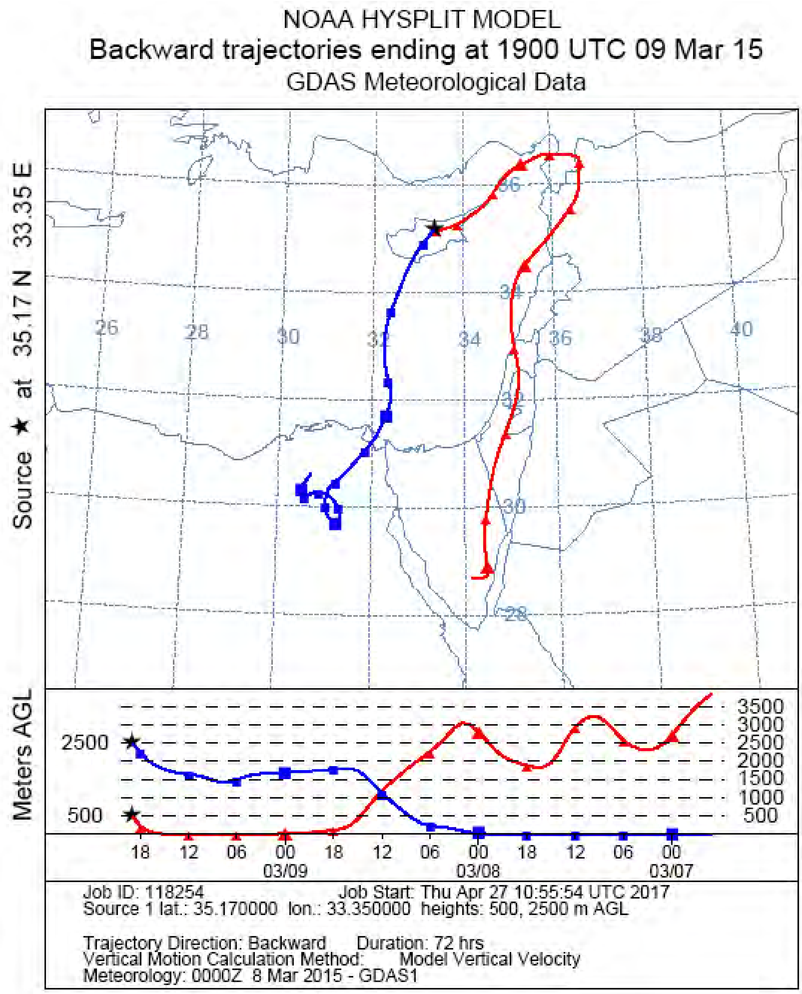

Figure 5.7: 3–day HYSPLIT backward trajectories arriving at Nicosia, Cyprus at 500 m (red) and 2500 m (blue) on March 9, 2015, 19.00 UTC (http://ready.arl.noaa.gov/HYSPLIT.php).

The air masses above originated from the north of Egypt, near the Mediterranean coast (blue trajectory). Although not belonging to the Arabian Peninsula, Egypt was affected by heavy dust outbreaks occuring in the beginning of March 2015 (see Chapter 2.2). A high fraction of dust particles in the layer between 1000 and 3800 m can be expected.

For a detailed inspection of the optical properties of the aerosol layers, a rather long measurement period from 18.00 to 22.30 UTC was chosen (red rectangle in Figure 5.6). In this way, signal noise within the dust layer with low concentration could be reduced. Profiles of the backscatter and extinction coefficient, as well as the lidar ratio, Ångström exponent and the particle linear depolarization ratio are shown in Figure 5.8.

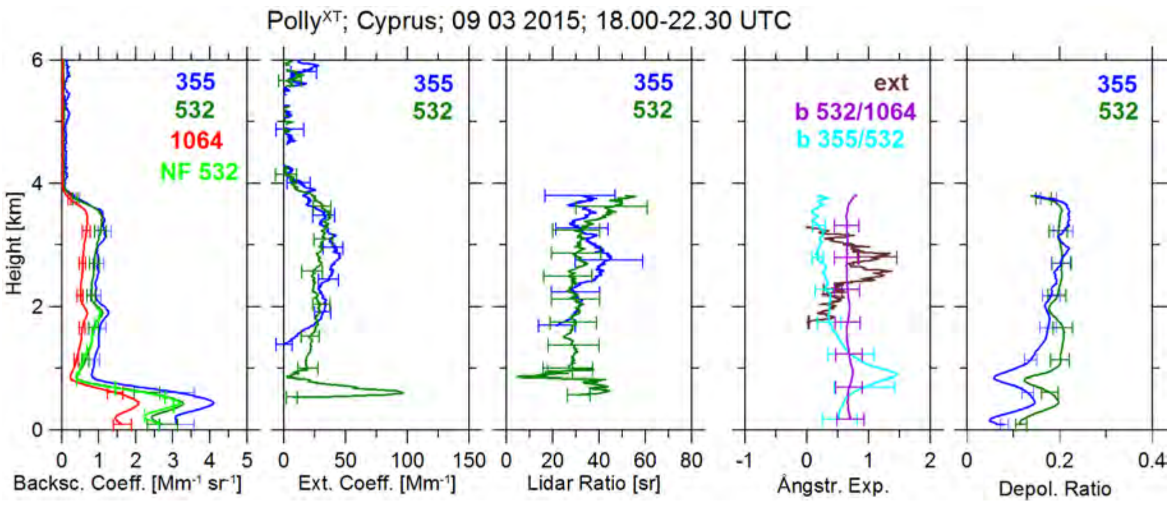

Figure 5.8: Profiles of the backscatter and extinction coefficient, lidar ratio, Ångström exponent and particle linear depolarization ratio (09.03.2015, 18.00–22.30 UTC, Nicosia, Cyprus). Applied vertical signal smoothing lengths: 187.5 m (backscatter coefficient, particle linear depolarization ratio, extinction coefficient up to 1 km, lidar ratio up to 1 km), 742.5 m (extinction coefficient and lidar ratio above 1 km, extinction–related Ångström exponent) and 367.5 m (backscatter–related Ångström exponents). Colors indicate profiles for the different wavelengths.

This time, the extinction coefficient and the lidar ratio were computed with a high vertical resolution of 187.5 m up to 1 km. Above 1 km, vertical signal smoothing lengths of 742.5 m were applied. The backscatter–related Ångström exponents were computed with a smoothing length of 367.5 m.
For the aerosol layer up to 700 m, a mean lidar ratio of 40±3 sr was calculated for 532 nm. Similar to the first case, marine particles seem to be mixed with dust particles from the layer above and/or dust from the days before. Mean particle linear depolarization ratios of 17±3 % (532 nm) and 12±3 % (355 nm) confirm these findings, suggesting an even greater amount of dust within the PBL than in the first case. Pollution from the coast might also play a role, leading to greater values of the lidar ratio compared to the first case. For the backscatter–related Ångström exponents, mean values of 0.6±0.1 (355/532) and 0.7±0.03 (532/1064) were calculated.

In the aerosol layer between 1 and 3.8 km, the particle linear depolarization ratio increases from lowest values of 11 % at 1 km height to highest values of 22.5 % at 3.5 km. Between 2 and 3.7 km, it remains almost constant and wavelength independent with mean values of 20±2 % (355 nm) and 20±1 % (532 nm), indicating a homogeneous aerosol layer.

Corresponding mean Ångström exponents of 0.5±0.3 (extinction–related), 0.3±0.1 (355/532) and 0.6±0.02 (532/1064) are slightly higher than typical values for pure dust found by Tesche et al. (2009). Mean lidar ratios of 36±11 sr (355 nm) and 31±7 sr (532 nm) are slightly below the range of observed values for aerosol layers containing Middle East desert dust by Nisantzi et al. (2015), reaching from 33 to 48 sr. The presence of marine particles from the Mediterranean Sea and pollution from Egypt within the elevated aerosol layer is very likely, leading to a decreased lidar ratio (marine particles), a decreased particle linear depolarization ratio (marine particles and pollution) and an increased Ångström exponent (pollution).

Althought a long measurement–period was considered for this case study, the lidar ratio shows quite large uncertainties, demonstrating the difficulty of the analysis of layers with low aerosol concentration.

5.3 Case Study: April 7, 2015

The third presented case was measured on April 7, 2015. In Figure 5.9, the time–height plot of the range–corrected signal at 1064 nm can be seen. It shows the arrival of a thick dust plume over Nicosia in the afternoon of April 7. In the evening, cloud formation can be noticed. The measurement period between 18.00 and 19.30 UTC, that was chosen for the detailed analysis of the aerosol optical properties, is characterized by an aerosol–containing PBL up to 700 m and a thick dust layer with a strong signal between 2 and 7 km.

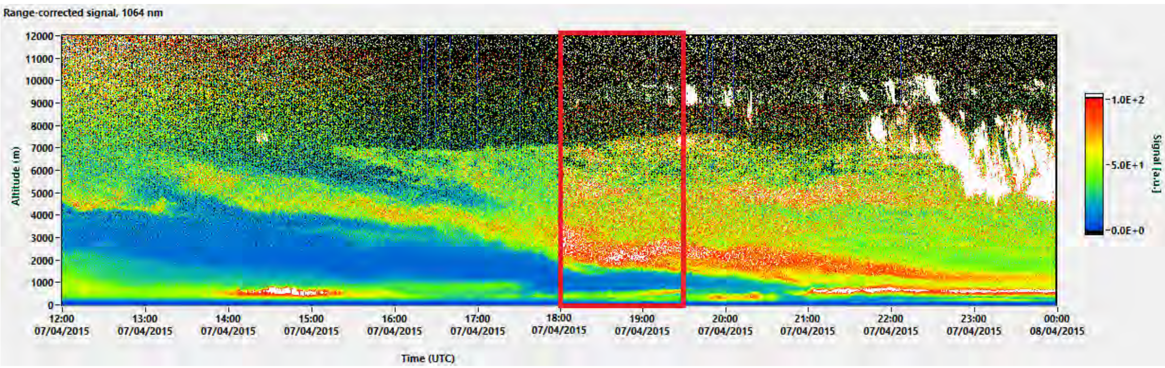

Figure 5.9: Time–height plot of the range–corrected signal at 1064 nm (07.04.2015, 12.00–00.00 UTC Nicosia, Cyprus)

According to the backward trajectories (Figure 5.10) arriving at 19 UTC at 2.5 km and 4 km height (blue and green trajectory), the dust layer originated from the Saharan Desert. The air masses were close to the ground over the Algerian Desert, belonging to the Sahara.

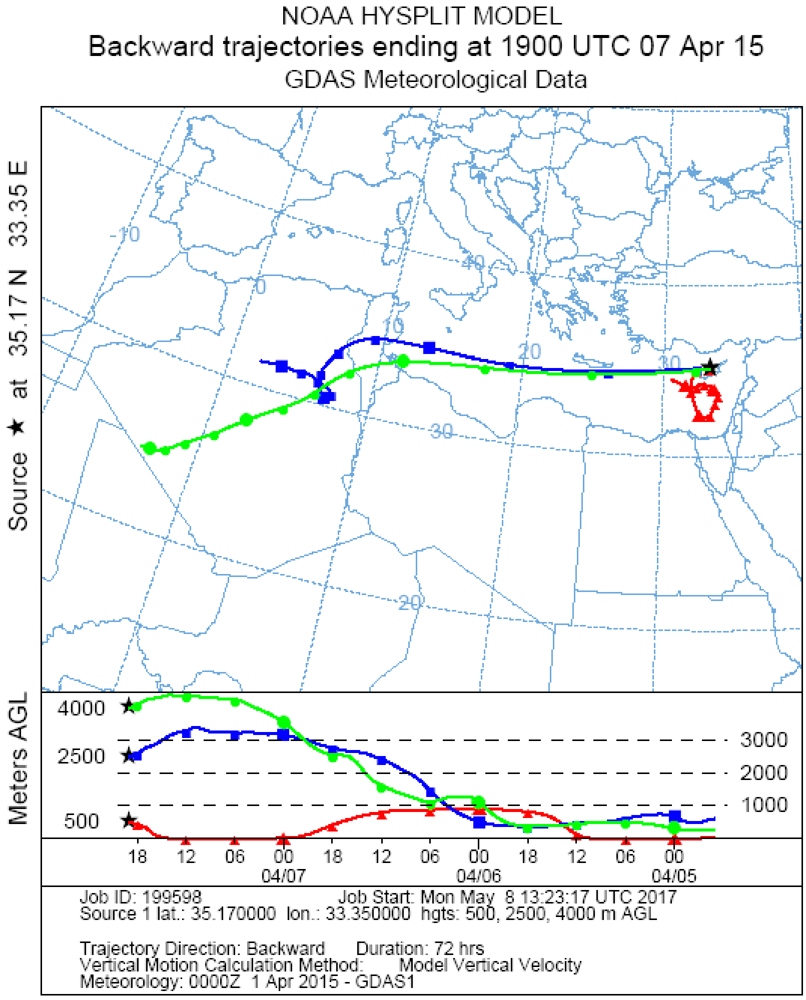

Figure 5.10: 3–day HYSPLIT backward trajectories arriving at Nicosia, Cyprus at 500 m (red), 2500 m (blue) and 4000 m (green) on April 7, 2015, 19.00 UTC (http://ready.arl.noaa.gov/HYSPLIT.php).

There, Saharan desert dust could be collected and then lifted to high altitudes on its way to Cyprus. This explains the high dust load at all heights up to 7 km in this case. The air masses of the PBL originated from the south of Cyprus. The corresponding red trajectory, arriving at 500 m, was close to the ground over the Mediterranean Sea. Therefore mainly marine particles are expected in the PBL.

Profiles of the optical properties of the observed aerosol layers are shown in Figure 5.11. This time, greater vertical smoothing lengths were applied before computing, in order to decrease signal noise in the upper part of the dust layer.

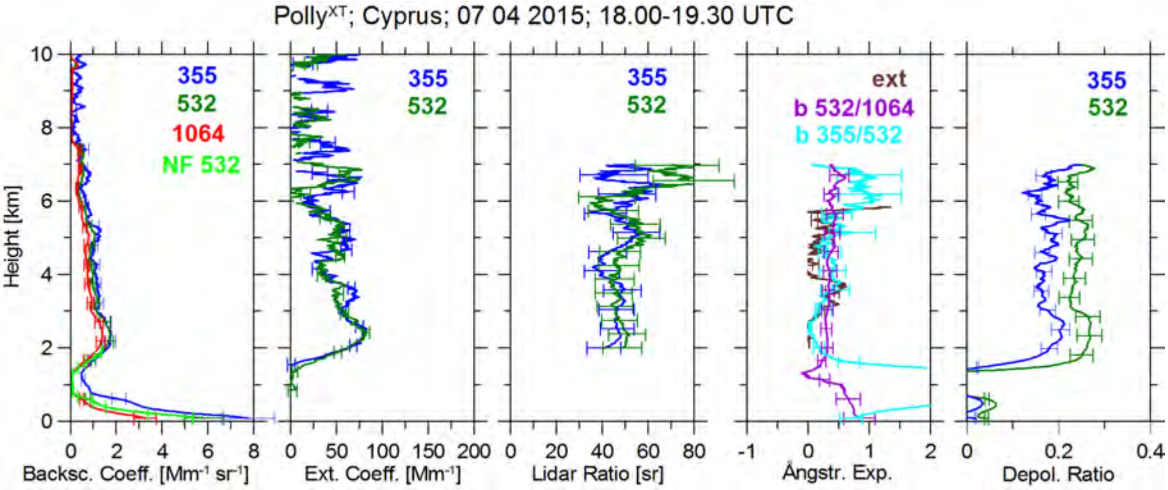

Figure 5.11: Profiles of the backscatter and extinction coefficient, lidar ratio, Ångström exponent and particle linear depolarization ratio (07.04.2015, 18.00–19.30 UTC, Nicosia, Cyprus). Vertical signal smoothing lengths: 187.5 m (backscatter coefficient, particle linear depolarization ratio and backscatter–related Ångström exponents (below 2 km)), 367.5 m (backscatter–related Ångström exponents above 2 km) and 742.5 m (extinction coefficient, lidar ratio and extinction–related Ångström exponent). Colors indicate profiles for the different wavelengths.

For the lidar ratio and the extinction coefficient, a vertical signal smoothing length of 742.5 m, was applied, as well as for the extinction–related Ångström exponent. Below 2 km, the backscatter–related Ångström exponents were computed with a high vertical resolution of 187.5 m, just as the backscatter coefficient and the particle linear depolarization ratio. Above 2 km, the backscatter–related Ångström exponents were computed with a vertical signal smoothing length of 367.5 m.

The 355 nm and 532 nm extinction coefficient profiles provide trustworthy values above 2 km height, showing almost wavelength independence throughout the dust layer.

For the aerosol layer within the PBL, only the backscatter–related Ångström exponents and the particle linear depolarization ratios are available. Mean values of 0.7±0.03 (532/1064) and 0.9±0.1 (355/532, from 100 to 300 m) and 5±1 % (532 nm) and 3±1 % (355 nm) were calculated. Low values of the particle linear depolarization ratio indicate the presence of spherical scatterers, such as marine aerosol particles. Due to the missing lidar ratio below 2 km height, no further statements can be made.

In the Saharan dust plume between 2 and 7 km height, the particle linear depolarization ratio remains almost constant with mean values of 19±2 % (355 nm) and 26±2 % (532 nm). The lidar ratio shows mean values of 48±6 sr and 50±10 sr for 355 and 532 nm. With mean values of 0.2±0.2 (extinction–related), 0.3±0.2 (355/532) and 0.4±0.1 (532/1064), the Ångström exponent deviates only slightly from found mean values for pure dust by Tesche et al. (2009). All parameters are in good agreement with findings of Nisantzi et al. (2015) for Saharan desert dust observed over Cyprus.

5.4 Case Study: April 9, 2015

The last presented case study is from April 9, 2015. In the time–height plot of the range–corrected signal at 1064 nm (Figure 5.12), an aerosol layer from surface up to 2500 m and several low– to mid–level clouds can be seen. No elevated aerosol layers were observed in this case.

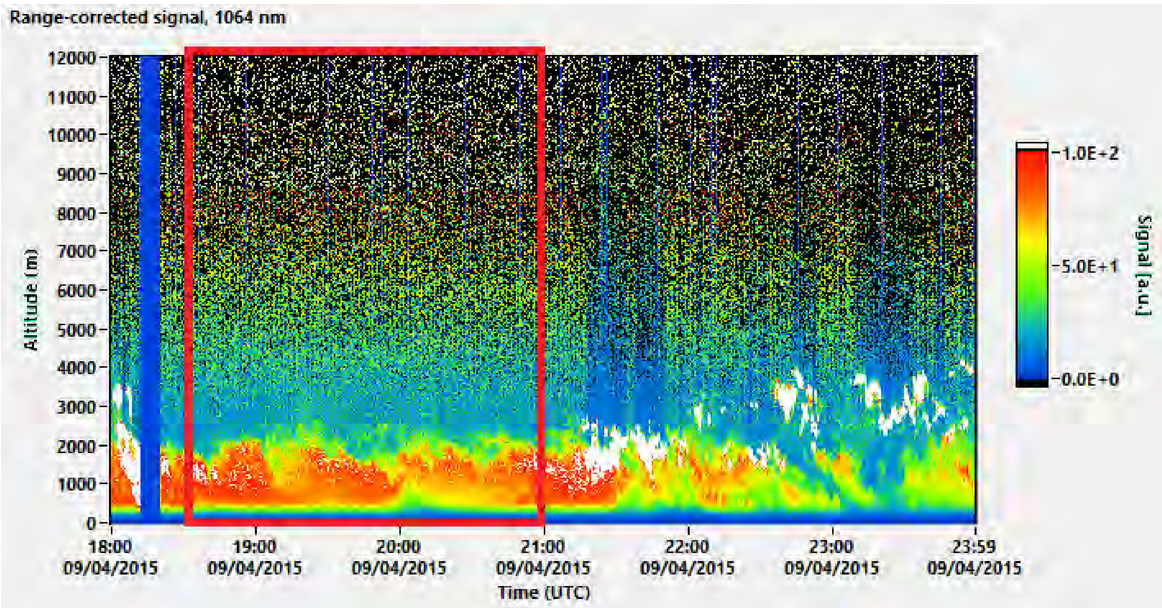

Figure 5.12: Time–height plot of the range–corrected signal at 1064 nm (09.04.2015, 18.00–00.00 UTC Nicosia, Cyprus)

In Figure 5.4, 2–day HYSPLIT backward trajectories arriving at Cyprus at 19 UTC are shown. The backward trajectories, arriving at 500 m (red) and 1000 m (blue), are almost identical and reach back to the northwest of Cyprus. The air masses were close to the ground over the Mediterranean Sea, to the west of Cyprus.

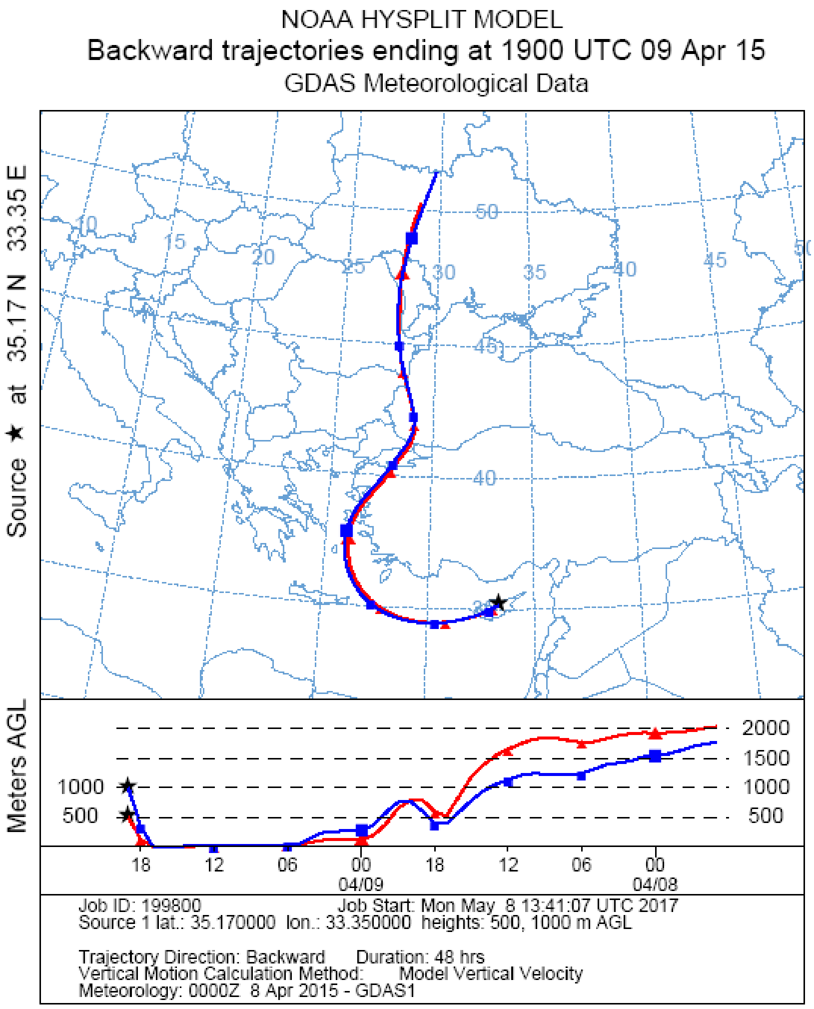

Figure 5.13: 2–day HYSPLIT backward trajectories arriving at Nicosia, Cyprus at 500 m (red) and 1000 m (blue) on April 9, 2015, 19.00 UTC (http://ready.arl.noaa.gov/HYSPLIT.php).

Mainly marine particles are expected at all heights throughout the observed aerosol layer.

The measurement period from 18.30 to 21.00 UTC (indicated by the red rectangle in Figure 5.12) was chosen for a detailed study of the aerosol optical properties. In Figure 5.14, profiles of the backscatter and extinction coefficient, as well as the lidar ratio, Ångström exponent and the particle linear depolarization ratio are shown. Before computing, the extinction coefficient and lidar ratio were smoothed with a vertical signal smoothing length of 367.5 m and all Ångström exponents with a smoothing length of 742.5 m.

For the lidar ratio, mean values of 19±7 sr (355 nm) and 23±5 sr (532 nm) were calculated.

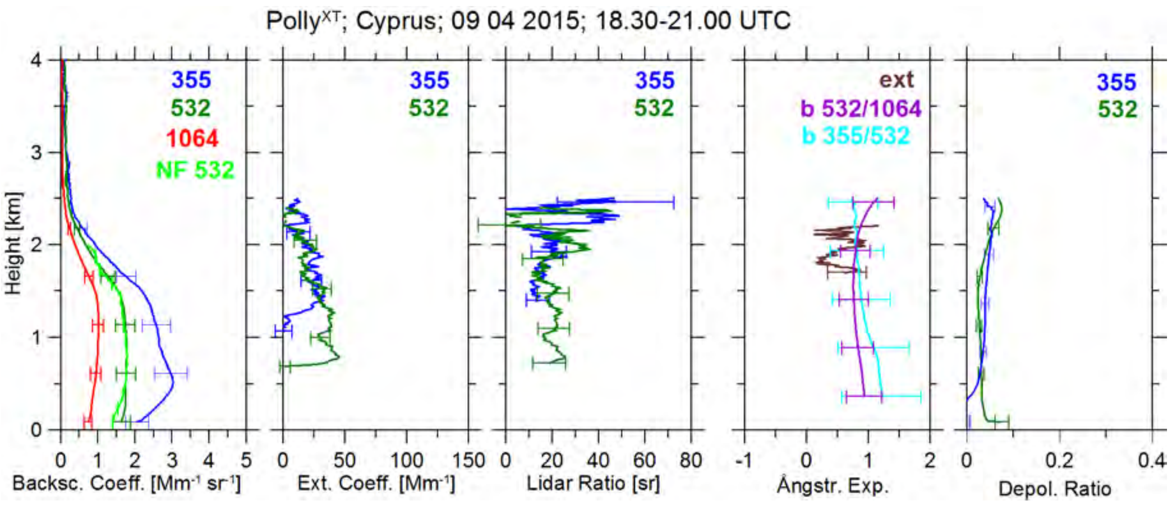

Figure 5.14: Profiles of the backscatter and extinction coefficient, lidar ratio, Ångström exponent and particle linear depolarization ratio (09.04.2015, 18.30–21.00 UTC, Nicosia, Cyprus). Vertical signal smoothing lengths: 187.5 m (backscatter coefficient and particle linear depolarization ratio), 367.5 m (extinction coefficient and lidar ratio) and 742.5 m (Ångström exponent). Colors indicate profiles for the different wavelengths.

The particle linear depolarization shows wavelength independence and an almost constant value troughout the aerosol layer. Mean values of 5±1 % (355 nm) and 4±2 % (532 nm) were calculated. For the Ångström exponent, mean values of 0.7±0.3 (extinction–related), 1.1±0.5 (355/532) and 1.0±0.2 (532/1064) were calculated.

The observed aerosol layer can thus be classified as clean marine layer.

5.5 Discussion

Four case studies were presented in this chapter, including observations of Middle East desert dust, Saharan desert dust, a complex dust mixture, mixtures of dust and marine aerosol, dust and pollution and clear marine aerosol layers. In this way, a good overview of typical aerosol conditions during the experiment was given. Differences between Middle East desert dust and Saharan desert dust lidar ratios as found by Nisantzi et al. (2015), could already be confirmed with the first and third case study. However, pure dust cases were rare during the experiment and mainly dust layers with a very low concentration as seen in the second case or dust mixtures were observed.

The described strategy of the case studies was applied for every measurement period of the entire campaign. Aerosol layers and their origins were identified for each case and mean values of the aerosol optical properties were calculated. In this way, a statistical analysis could be developed that will be presented in the next chapter.

Chapter 6

Results – Part II: Statistical Analysis

6.1 Overview

During the BACCHUS–Cyprus campaign, lidar measurements were performed on 43 days. As the high level of sky background light prohibits the detection of Raman signals with low signal noise, only late evening measurement periods were selected to be able to apply the Raman–Lidar–Method. Due to start problems and rainfall, some measurement days had to be eliminated. In a few cases, thick cloud layers made it impossible to find a reference height for the Raman–Lidar–Method, so that these measurement periods had to be left out as well. In the end, 32 measurement periods could be included in the statistical analysis. In Table 6.1 and Table 6.2, the observed aerosol layers of the 32 measurement periods are listed. The date and time of the measurement periods, as well as the base and top height of the aerosol layers and their thickness is listed. Furthermore, a suggestion for the aerosol type is given for each aerosol layer. As described in the previous chapter, backward trajectories were used to identify the origin of the detected air masses. Moreover, information on dust outbreaks and fire activity was helpful to determine the aerosol type. Some aerosol layers were separated into two or more aerosol layers, according to the backward trajectories and thus their composition of aerosol particles. Altogether, 59 aerosol layers could be analysed. Most of the time, not only one but two or more different aerosol layers were present during a measurement period. Various aerosol types could be identified: marine particles (mar.), Middle East desert dust (ME dust), Saharan desert dust (Sah.dust), pollution (poll.) and smoke. Observed aerosol layers of only one aerosol type were rare, mainly mixtures of two or three aerosol types were observed. In almost all cases, the aerosol types of these complex mixtures could be distinguished. Only one mixture remains uncertain, labeled as 'mix' in Table 6.1. This Middle East desert dust mixture was already presented in Chapter 5.1.

Table 6.1: Observed aerosol layers during the BACCHUS–Cyprus campaign (March 2015). Date and time of the measurement period, base, top and thickness of the aerosol layer and suggested aerosol type. A low concentration of aerosol within the observed layer is labeled with (lc).

Date	Time [UTC]	Base [km]	Top [km]	Thickness [km]	Aerosol Type
06.03.2015	20.17–21.29	0.1	1.9	1.8	marine
07.03.2015	19.00–21.00	0.1	1.1	1.0	marine+dust
07.03.2015	19.00–21.00	1.1	1.7	0.6	ME dust
07.03.2015	19.00–21.00	1.7	2.6	0.9	ME dust mix
08.03.2015	19.20–21.20	0.2	1.4	1.2	marine+dust
09.03.2015	18.00–22.30	0.1	0.7	0.6	marine+dust
09.03.2015	18.00–22.30	1.0	3.8	2.8	ME dust+poll. (lc)
12.03.2015	20.55–22.10	0.1	1.9	1.8	marine
13.03.2015	18.00–19.20	0.2	1.9	1.7	marine
14.03.2015	18.30–20.30	0.1	2.0	1.9	marine+dust
14.03.2015	18.30–20.30	3.5	5.0	1.5	Sah.dust+mar.(lc)
15.03.2015	18.30–20.30	0.1	2.0	1.9	marine
16.03.2015	18.30–20.30	0.1	2.0	1.9	marine+poll.
16.03.2015	18.30–20.30	2.0	2.5	0.5	pollution
17.03.2015	22.00–23.00	0.1	2.5	2.4	marine+poll.
17.03.2015	22.00–23.00	6.0	10.0	4.0	Sah.dust
18.03.2015	18.35–19.10	0.1	1.9	1.8	marine+poll.
18.03.2015	18.35–19.10	2.3	6.0	3.7	Sah.dust+poll.(lc)
19.03.2015	20.05–21.05	0.1	2.1	2.0	marine+poll.
19.03.2015	20.05–21.05	5.0	7.0	2.0	Sah.dust+poll.(lc)
21.03.2015	21.00–23.35	0.1	1.8	1.7	marine
22.03.2015	19.00–21.00	0.1	0.7	0.6	marine+poll.
22.03.2015	19.00–21.00	2.0	6.0	4.0	Sah.dust+poll.(lc)
24.03.2015	19.40–21.20	0.2	1.0	0.8	marine+poll.
24.03.2015	19.40–21.20	1.1	2.3	1.2	Sah.dust+mar.(lc)
24.03.2015	19.40–21.20	2.8	5.0	2.2	Sah.dust+marl.(lc)
25.03.2015	21.45–23.45	0.1	1.5	1.4	marine+poll.
25.03.2015	21.45–23.45	3.0	6.0	3.0	Sah.dust+poll.(lc)
26.03.2015	18.30–20.30	0.2	2.2	2.0	mar.+poll.+smoke
26.03.2015	18.30–20.30	2.2	6.0	3.8	Sah.dust+smoke
28.03.2015	18.30–20.30	0.1	2.6	2.5	marine+dust
28.03.2015	18.30–20.30	2.6	4.0	1.4	Sah.dust+poll.(lc)
29.03.2015	18.30–20.30	0.1	3.0	2.9	marine+dust
30.03.2015	18.30–20.30	0.1	1.3	1.2	marine+dust

Table 6.2: Observed aerosol layers during the BACCHUS–Cyprus campaign (April 2015). Date and time of the measurement period, base, top and thickness of the aerosol layer and suggested aerosol type. A low concentration of aerosol within the observed layer is labeled with (lc).

Date	Time [UTC]	Base [km]	Top [km]	Thickness [km]	Aerosol Type
01.04.2015	22.40–23.40	0.1	1.1	1.0	marine
01.04.2015	22.40–23.40	1.1	4.0	2.9	marine+poll. (lc)
02.04.2015	20.00–21.30	0.1	1.9	1.8	marine
03.04.2015	21.50–23.50	0.1	2.0	1.9	marine
03.04.2015	21.50–23.50	2.0	5.0	3.0	pollution (lc)
04.04.2015	18.00–20.00	0.1	1.3	1.2	marine+poll.
04.04.2015	18.00–20.00	1.3	6.0	4.7	pollution (lc)
05.04.2015	21.50–23.50	0.1	1.2	1.1	marine
05.04.2015	21.50–23.50	3.0	5.0	2.0	marine+poll.(lc)
06.04.2015	18.10–19.20	0.1	1.0	0.9	marine
06.04.2015	18.10–19.20	1.0	2.0	1.0	marine+dust.
06.04.2015	18.10–19.20	2.0	4.0	2.0	Sah.dust+marine
06.04.2015	18.10–19.20	4.0	7.0	3.0	Sah.dust+poll.(lc)
07.04.2015	18.00–19.30	0.1	0.7	0.6	marine
07.04.2015	18.00–19.30	2.0	7.0	5.0	Sah.dust
08.04.2015	22.50–23.50	0.1	1.8	1.7	marine+dust
08.04.2015	22.50–23.50	1.8	3.5	1.7	Sah.dust
09.04.2015	18.30–21.00	0.1	2.5	2.4	marine
11.04.2015	20.10–21.30	0.1	2.0	1.9	marine
11.04.2015	20.10–21.30	2.0	4.0	2.0	pollution (lc)
12.04.2015	19.00–20.05	0.2	2.0	1.8	marine+poll.
12.04.2015	19.00–20.05	2.0	2.4	0.4	smoke+poll.
12.04.2015	19.00–20.05	2.4	5.0	2.6	pollution (lc)
13.04.2015	18.00–19.15	0.1	2.5	2.4	marine+poll.
13.04.2015	18.00–19.15	2.5	6.0	3.5	pollution (lc)

Numerous aerosol layers with a low concentration (lc) of aerosol were detected. As already described in Chapter 5.2, a low concentration of aerosol particles leads to an increased signal noise and thus large uncertainties. In the next section, different time series will be presented. Besides the above–described aerosol layer vertical extension, the temporal change of the aerosol optical properties will be discussed.

6.2 Time Series

Figure 6.1 shows the vertical extension of all analyzed aerosol layers during the experiment. Aerosol layers within the planetary boundary layer and elevated aerosol layers are indicated by blue and black bars, respectively. For an obvious distinction between the different aerosol layers of each measurement period, thin white lines were inserted, even though a continuous transition between the aerosol layers occurred in many cases. Top heights of the PBL–aerosol layers are in the range between 0.7 and 3 km and the aerosol layer thickness varies from 0.6 to 2.9 km. The elevated aerosol layers show greater differences in height and thickness. A maximum top height of 10 km and a minimum top height of 1.7 km was observed. The layer thickness is in the range between 0.4 and 5 km.

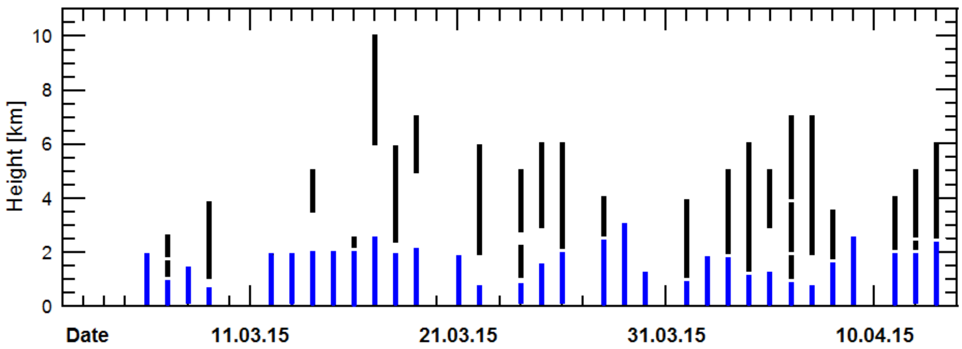

Figure 6.1: Time series of the vertical extension of all observed aerosol layers of the PBL (blue) and elevated aerosol layers (black)

Mean values for the particle backscatter and extinction coefficient, lidar ratio, particle linear depolarization ratio and Ångström exponent were calculated for every observed aerosol layer. Time series of these parameters are shown in the following figures. Mean values for the observed aerosol layers within the planetary boundary layer are plotted as blue dots, whereas elevated aerosol layers are indicated by black circles in each figure. The standard deviation is indicated by error bars. It is affected by atmospheric variability as well as by measurement uncertainties. During analysis, different vertical signal smoothing lengths were used, 187.5 m for the backscatter coefficient and the particle linear depolarization ratio and 367.5 m for all other parameters.

In Figure 6.2, the temporal change of the backscatter coefficient at 355, 532 and 1064 nm can be seen. Apart from three cases (March 7, March 26 and April 8), the backscatter coefficient for the aerosol layers within the planetary boundary layer was obviously higher than the values for the elevated layers.

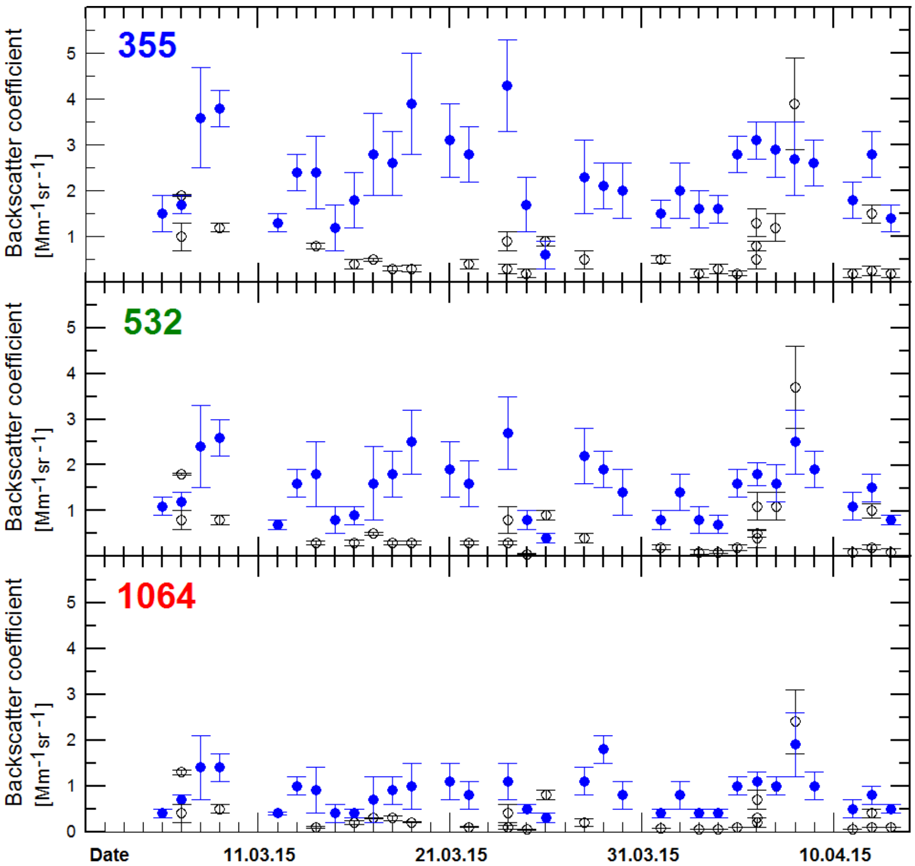

Figure 6.2: Mean values of the backscatter coefficient at 355, 532 and 1064 nm for the analyzed aerosol layers in the planetary boundary layer (blue dots) and elevated aerosol layers (black circles). Error bars indicate the standard deviation.

The spread ranges from 0.6 to 4.3 $Mm^{-1}sr^{-1}$ (355 nm), 0.4 to 2.7 $Mm^{-1}sr^{-1}$ (532 nm) and 0.3 to 1.9 $Mm^{-1}sr^{-1}$ (1064 nm) for the PBL–aerosol layers. For the elevated aerosol layers mean values in the range from 0.2 to 1.9 $Mm^{-1}sr^{-1}$ (355 nm), 0.05 to 1.8 $Mm^{-1}sr^{-1}$ (532 nm) and 0.05 to 1.3 $Mm^{-1}sr^{-1}$ (1064 nm) were calculated. Mean values for the elevated aerosol layer on April 8 are significantly higher with 3.9 ± 1.0 $Mm^{-1}sr^{-1}$ (355 nm), 3.7 ± 0.9 $Mm^{-1}sr^{-1}$ (532 nm) and 2.4 ± 0.7 $Mm^{-1}sr^{-1}$ (1064 nm). As already discussed in the previous chapter, a thick Saharan dust plume arrived at Cyprus in the afternoon of April 7, 2015. The dust particles were subsequently mixed downward and compressed, causing comparatively high backscatter and extinction coefficients on April 8, which can be also seen in Figure 6.3. However, the time series of the particle backscatter coefficient documents a huge amount of aerosol particles within the PBL during the entire campaign and the presence of many elevated aerosol layers with a low aerosol concentration.

The time series of the extinction coefficient (Fig 6.3) appears similar. Mean values for the PBL–aerosol layers are obviously higher than for the elevated aerosol layers in most cases. Due to the incomplete overlap, some extinction coefficients at 355 nm are missing, so that only trustworthy values appear in the time series. Mean values are in the range from 7 to 138 Mm^{-1} (355 nm) and from 10 to 111 Mm^{-1} (532 nm) for the PBL–aerosol layers and from 2 to 86 Mm^{-1} (355 nm) and 2 to 75 Mm^{-1} (532 nm) for the elevated aerosol layers. Again, the values for the elevated aerosol layer on April 8 differ strongly from all other cases, showing mean extinction coefficients of 217±68 Mm^{-1} (355 nm) and 210±69 Mm^{-1} (532 nm).

Mean values of the lidar ratio are shown in Figure 6.4. Missing extinction coefficients at 355 nm led to missing lidar ratios at 355 nm in some cases. For the PBL–aerosol layers the lidar ratio ranges from 15 to 50 sr (355 nm) and from 19 to 50 sr (532 nm), exept for one single case (March 26) where significantly higher mean values of 67±29 sr (355 nm) and 71±23 sr (532 nm) were calculated. This was the only observation of smoke in the PBL, reaching Cyprus from the Ukraine, together with anthropogenic pollution and marine particles from the Mediterranean and Black Sea.

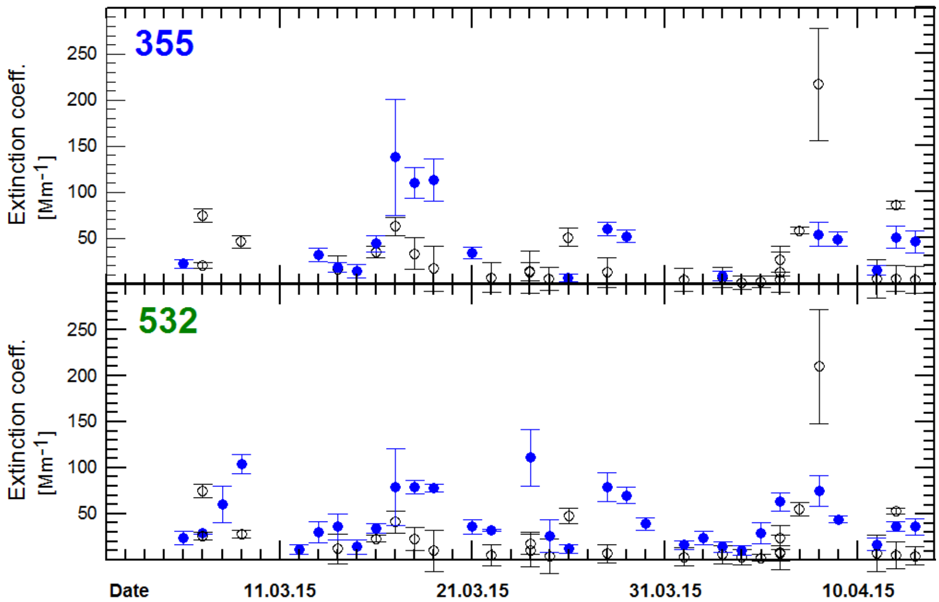

Figure 6.3: Mean values of the extinction coefficient at 355 and 532 nm for the analyzed aerosol layers in the planetary boundary layer (blue dots) and elevated aerosol layers (black circles). Error bars indicate the standard deviation.

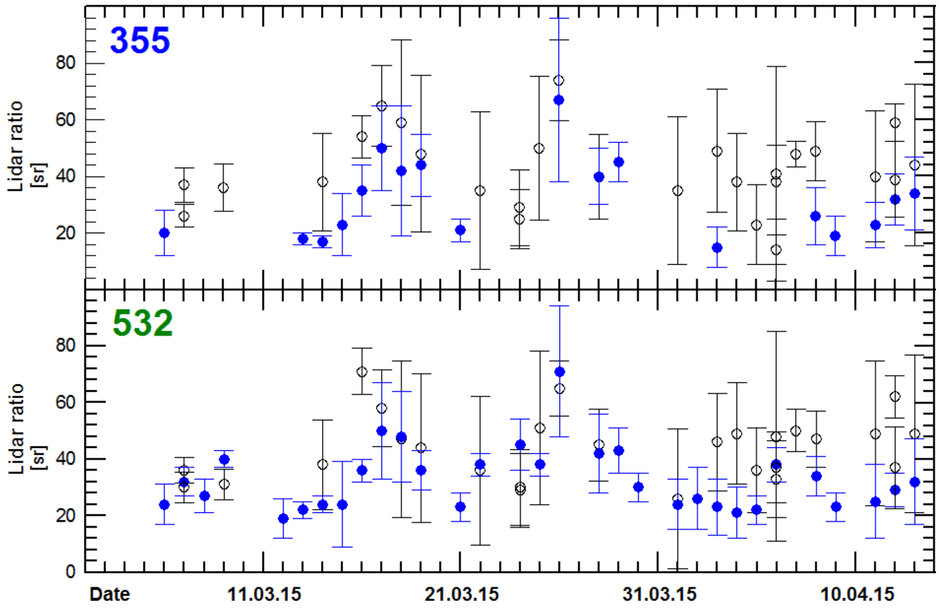

Figure 6.4: Mean values of the lidar ratio at 355 and 532 nm for the analyzed aerosol layers in the planetary boundary layer (blue dots) and elevated aerosol layers (black circles). Error bars indicate the standard deviation.

Some clear marine cases occured with lidar ratios of about 20 sr, but most of the time marine particles were mixed with mineral dust and/or pollution, leading to increased lidar ratios. For the elevated aerosol layers, mean lidar ratios between 23 and 74 sr (355 nm) and between 26 and 71 sr (532 nm) were calculated. The standard deviation, indicated by error bars in Figure 6.4, is quite large in many cases. Rather inhomogeneous mixtures of different aerosol types lead to a high variability of values for the lidar ratio. In addition, low concentrations of aerosol particles within the elevated aerosol layers cause a high signal noise. However, almost pure dust cases during heavy dust outbreaks show only small uncertainties, as seen on March 7, March 17 and April 7.

In Figure 6.5, the temporal change of the particle linear depolarization ratio can be seen. Mean values for the PBL–aerosol layers were usually below 10 %, which is typical for almost spherical particles, such as marine particles, pollution or smoke. In some cases, the particle linear depolarization ratio was increased, indicating the presence of mineral dust. In the majority of cases, residual Middle East or Saharan desert dust from the days before and/or concurrent dust layers above was mixed downward into the PBL. Another source for an increased particle linear depolarization ratio could be the presence of local dust from the island of Cyprus itself.

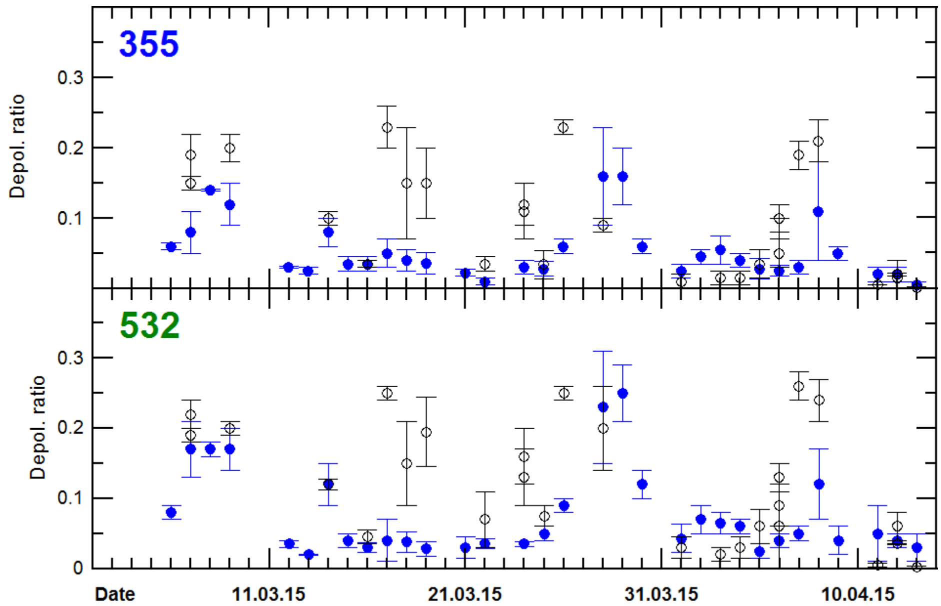

Figure 6.5: Mean values of the particle linear depolarization ratio at 355 and 532 nm for the analyzed aerosol layers in the planetary boundary layer (blue dots) and elevated aerosol layers (black circles). Error bars indicate the standard deviation.

Mean values for the PBL–aerosol layers are in the range between 1 and 16 % (355 nm) and 2 and 25 % (532 nm). Elevated aerosol layers show a greater variability of the particle linear depolarization ratio with mean values in the range from 0.1 to 23 % (355 nm) and from 0.2 to 26 % (532 nm).

The time series of the Ångström exponent is shown in Figure 6.6. In the upper panel, the temporal change of the extinction–related Ångström exponent is presented, whereas the backscatter–related Ångström exponents can be seen in the panels below.
Due to missing extinction coefficients at 355 nm, the extinction–related Ångström exponent shows less values than the backscatter–related Ångström exponents with calculated mean values in the range from 0.1 to 1.5 for the PBL– aerosol layers and from 0.2 to 1.8 for elevated aerosol layers. The Ångström exponent, calculated with the backscatter coefficient at 355 and 532 nm, shows mean values between 0.4 and 1.9 for the PBL–aerosol layers and between 0.03 and 1.8 for elevated aerosol layers. The Ångström exponent, calculated with the backscatter coefficient at 532 and 1064 nm shows mean values in the range from 0.1 to 1.4 for the PBL and from 0.18 to 1.9 for elevated aerosol layers. Three values differ from this range, showing significantly higher values of the Ångström exponent of the elevated aerosol layers of 2.1±0.9 (April 1), 2.8±1.1 (April 3) and 2.1±0.6 (April 4).

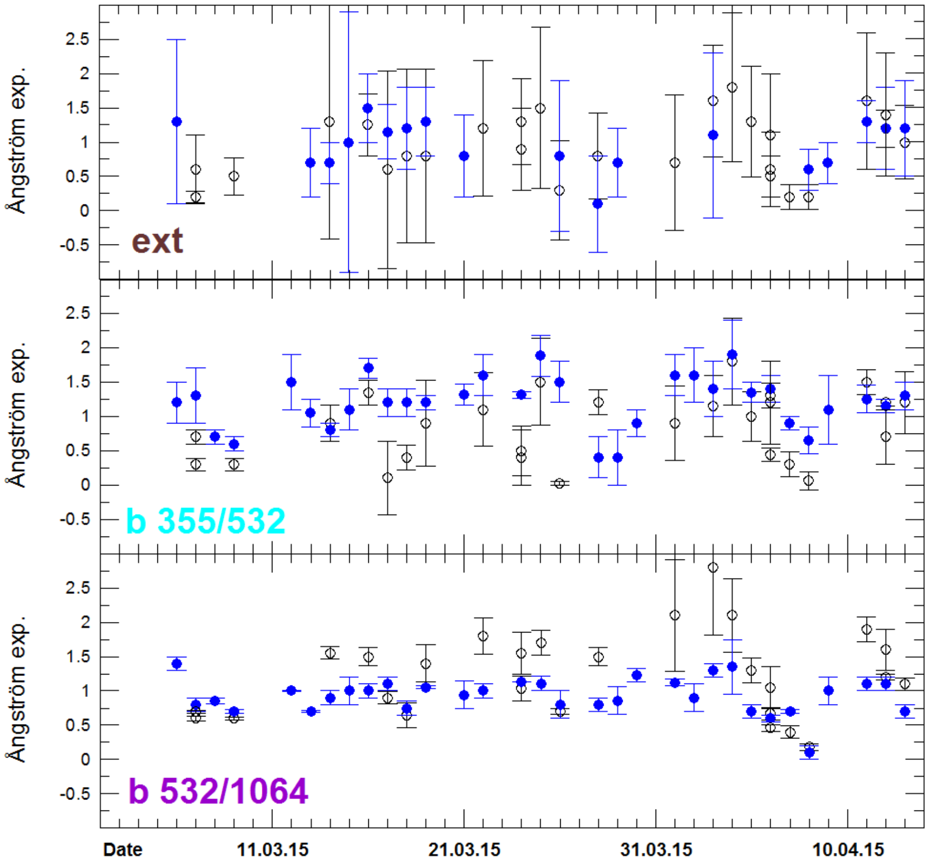

Figure 6.6: Mean values of the Ångström exponent for the analyzed aerosol layers in the planetary boundary layer (blue dots) and elevated aerosol layers (black circles). Error bars indicate the standard deviation.

During these days, almost pure anthropogenic pollution from central, western and southern parts of Europe (France, Germany, Italy) reached Cyprus. The concentration of particles was rather low, leading to high uncertainties compared to all other mean values. However, the time series of the Ångström exponent shows decreased mean values in cases of large dust particles during dust outbreaks (e.g. March 7, April 7 and April 8) and increased mean values for smaller particles like pollution and smoke (e.g. April 4, April 11 and April 12). Marine particles vary in size and thus show a quite large spread of mean values for the Ångström exponent.

In the next section, the calculated mean values for the lidar ratio, the particle linear depolarization ratio and the Ångström exponent will be combined to characterize the different observed aerosol types.

6.3 Aerosol Characterization

The lidar ratio, the particle linear depolarization ratio and the Ångström exponent are intensive quantities, meaning that they do not depend on the amount of particles. Thus, they are convenient quantities for the characterization of different aerosol types. In this section, the calculated mean values of these quantities, presented in the preceding section, will be allocated to the aerosol types and mixtures of all observed aerosol layers.

All quantities are illustrated against each other, starting with the lidar ratio and the particle linear depolarization ratio (Figure 6.7). In the first row of Figure 6.7, the calculated mean values of the lidar ratio at 355 nm (532 nm) are plotted as a function of the particle linear depolarization ratio at 355 nm (532 nm) for all observed PBL–aerosol layers (blue dots) and all elevated aerosol layers (black dots). It can be already noticed, that the PBL–aerosol layers frequently show low mean values for the lidar ratio and the particle linear depolarization ratio, indicating the presence of marine particles, whereas values for the elevated aerosol layers are more dispersed. For each plotted dot, the aerosol type was identified, which can be seen in the second row of Figure 6.7. A distinction was made between almost pure aerosol types and mixtures. The air masses of each aerosol layer were analyzed by means of backward trajectories. Air masses that were only close to the ground over the sea and that were not influenced by turbulent mixing processes with concurrent dust or pollution layers, were classified as pure marine. In the lower panels of Figure 6.7, mean values for these air masses are plotted with a blue background. Backward trajectories reaching back to desert areas during times of dust outbreaks were an indicator for pure Saharan (Sah) or Middle East (ME) dust. Again, only confined dust layers were classified as pure dust layers to be able to exclude considerable mixing with other particles. Mean values for these aerosol layers appear with a yellow (ME) or orange (Sah) background in Figure 6.7. Cases with almost pure anthropogenic pollution were identified in the same way. Air masses, originating from urban conglomerations, that were not close to the ground over the sea and did not pass desert areas or areas with remarkable fire activity, were classified as polluted. These are plotted with a grey background in Figure 6.7. Pure smoke could not be observed during the campaign.

All above–described aerosol layers of one dominating aerosol type are named pure, being aware that the presence of other components within these layers can not be completely excluded.

Mixtures of two or three aerosol types are plotted with a white background in Figure 6.7 (lower panels). Mean values for the observed mixtures are surrounded by colored ovals. In this way, the presence of the different aerosol types within a mixture is simulated. At first sight, Figure 6.7 might appear kind of cluttered, due to the fact that a manifold variation of mixtures was observed, but actually it represents the aerosol situation at the island of Cyprus as it is: rather complex. Pure cases are quite rare and the presence of aerosol mixtures prevails. Altogether, 9 different mixtures could be observed during the campaign. Marine particles were frequently mixed with pollution or dust, mainly Saharan dust. One mixture of marine particles, pollution and smoke could be observed.

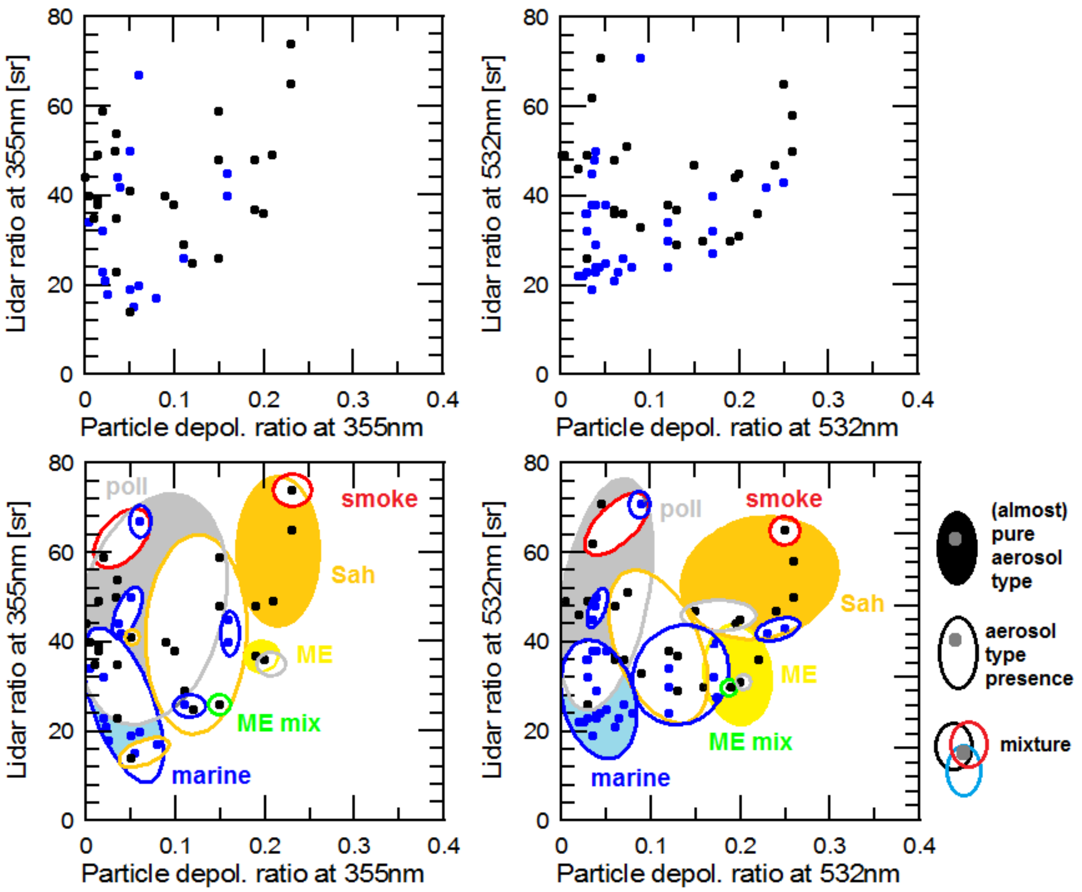

Figure 6.7: First row: Lidar ratio vs. particle linear depolarization ratio at 355 nm (left) and 532 nm (right) for all analyzed aerosol layers in the planetary boundary layer (blue dots) and elevated aerosol layers (black dots). Second row: same figures, but with delineated aerosol classification. A colored background indicates the observation of one (almost pure) aerosol type, a white background the observation of a mixture. Colored ovals show which aerosol types appear in the mixtures.

Several aerosol layers containing pollution and Saharan dust were observed, whereas a mixture of pollution and Middle East dust only occurred in one case. A mixture of smoke and pollution was observed during one measurement period, as well as a mixture of smoke and Saharan dust. One undefined mixture of Middle East dust and other particles appeared, surrounded by a green oval in Figure 6.7. Lowest values of the lidar ratio together with low values of the particle linear depolarization ratio were observed for marine particles. Mixing with dust particles led to higher values of both quantities with the exception of three cases, showing lower lidar ratios at 355 nm. Marine particles mixed with pollution still showed low values of the particle linear depolarization ratio, but an enhanced lidar ratio. The lidar ratio for pollution was significantly higher than for marine particles. The presence of smoke led to a further increase of the lidar ratio with no remarkable change of the particle linear depolarization ratio. Saharan dust showed high values of both quantities. Mixing with pollution led to significantly lower values of the particle linear depolarization ratio, but an only minor decrease of the lidar ratio. All these findings are in good agreement with previous studies. The behavior of the lidar ratio and the particle linear depolarization ratio of two different aerosol types in a mixture was already discussed by Groß et al. (2013). It was found out that the values of the lidar ratio (particle linear depolarization ratio) of the mixtures are between the values of the lidar ratio (particle linear depolarization ratio) of the pure aerosol types. Furthermore, it was noticed that a huge amount of aerosol type x compared to aerosol type y within the mixture leads to a clear tendency to values of the lidar ratio and the particle linear depolarization ratio of aerosol type x. This behavior could be monitored by means of Figure 6.7.

Figure 6.7 also demonstrates differences between Middle East and Saharan dust. The latter showed considerably greater values of the lidar ratio and somewhat higher values of the particle linear depolarization ratio. A detailed list of all observed aerosol types and mixtures is provided in Table 6.3 and Table 6.4 at the end of this chapter. There, calculated values of the lidar ratio and the particle linear depolarization ratio are presented together with values of the Ångström exponent.

In Figure 6.8, the Ångström exponent (backscatter–related as well as extinction–related) is plotted against the lidar ratio at 355 nm and 532 nm. As in Figure 6.7, values for the PBL–aerosol layers are indicated by blue dots and values for the elevated aerosol layers by black dots. The different images show plots at different wavelengths. It can be noticed, that all plots appear quite similar, showing a wide spread of values. Marine particles with a lidar ratio of about 20 sr frequently had an Ångström exponent of about 1.

Large particles are characterized by small Ångström exponents, but can not be directly associated with dust particles by means of the presented plots, due to the wide spread of the lidar ratio. High values of the lidar ratio together with high values of the Ångström exponent indicate the presence of small particles such as pollution or smoke.

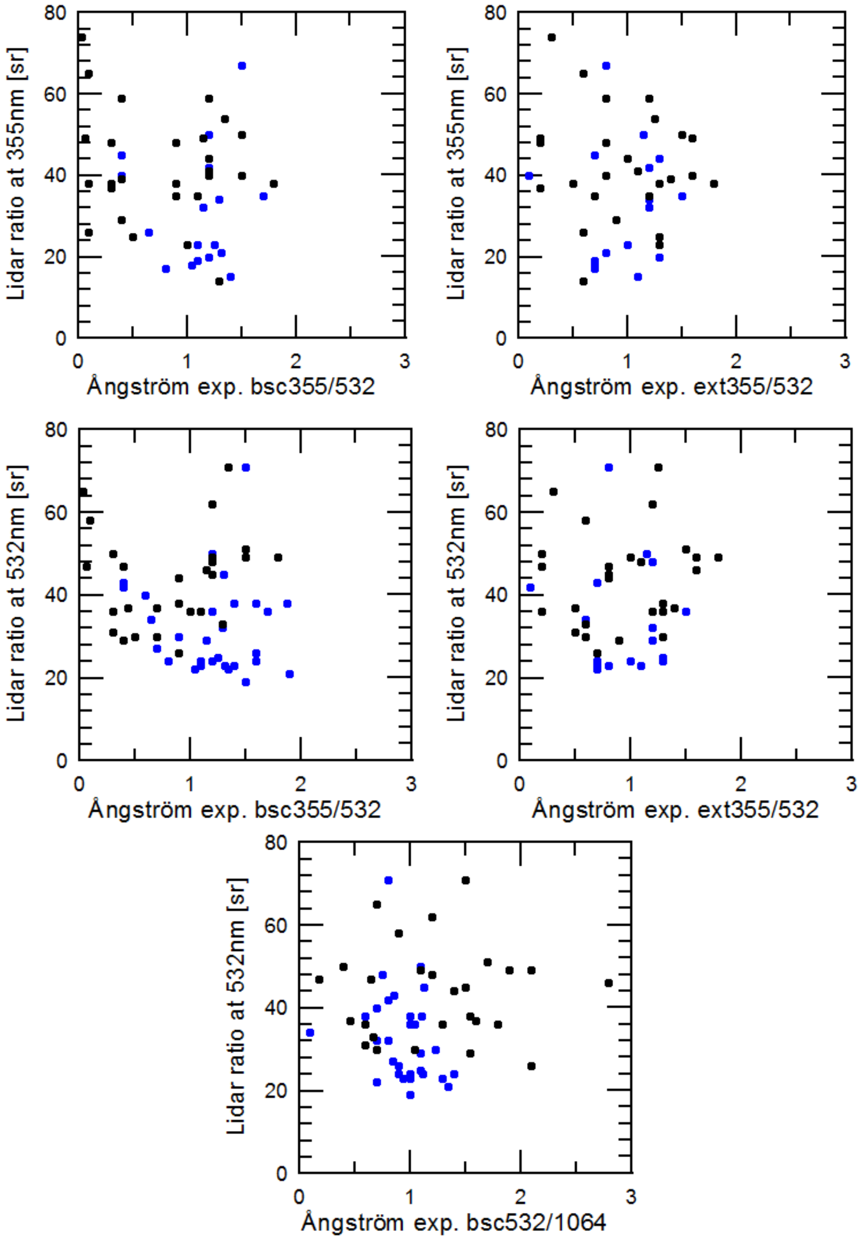

Figure 6.8: Lidar ratio at 355 nm (first row) and at 532 nm (second and third row) vs. Ångström exponent (355/532 extinction and 355/532 and 532/1064 backscatter) for all analyzed aerosol layers in the planetary boundary layer (blue dots) and elevated aerosol layers (black dots).

Figure 6.9 shows the Ångström exponent plotted against the particle linear depolarization ratio. Smallest values of the Ångström exponent were observed for particles with the highest particle linear depolarization ratio. These can be clearly identified as dust particles.

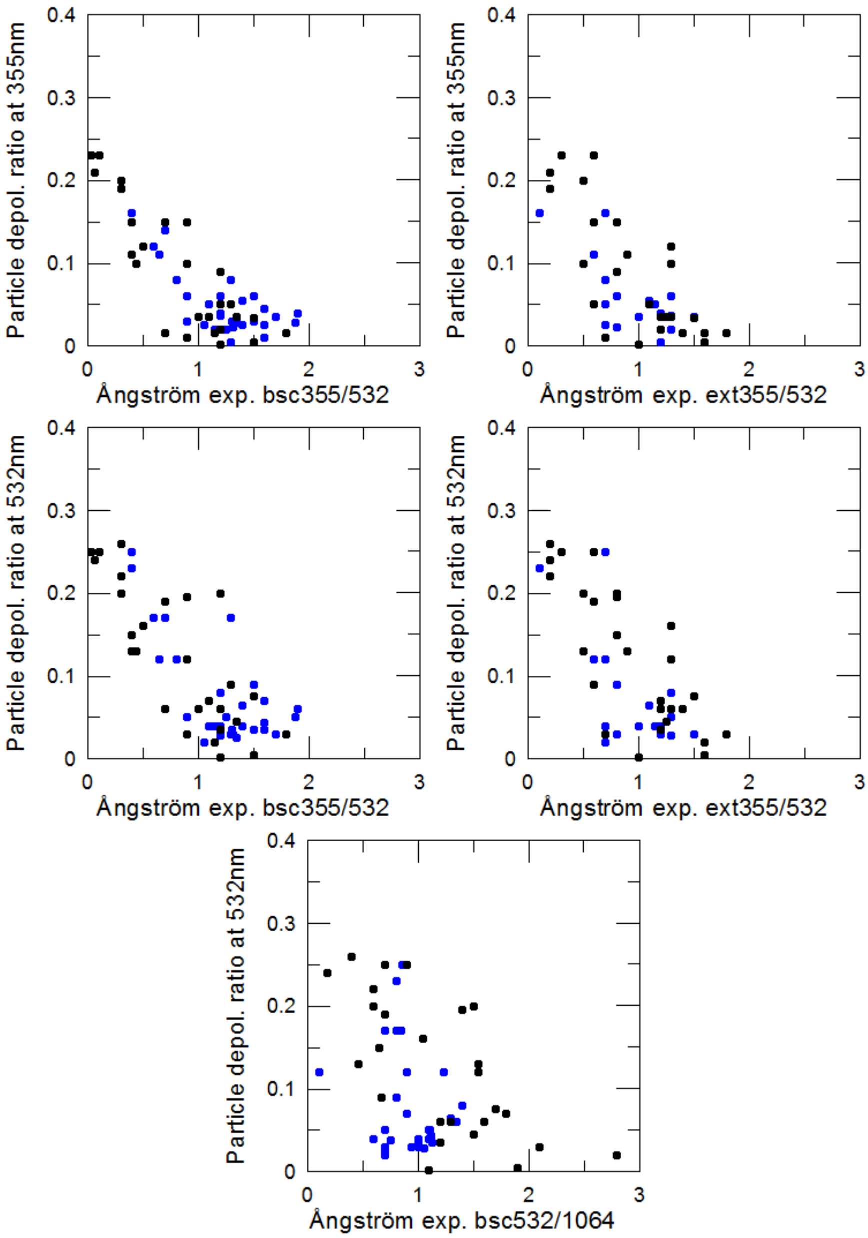

Figure 6.9: Particle linear depolarization ratio at 355 nm (first row) and at 532 nm (second and third row) vs. Ångström exponent (355/532 extinction and 355/532 and 532/1064 backscatter) for all analyzed aerosol layers in the planetary boundary layer (blue dots) and elevated aerosol layers (black dots).

Mixtures of dust with other particles showed a decrease of the particle linear depolarization ratio and an increase of the Ångström exponent. For particles with a low particle linear depolarization ratio such as marine particles, pollution and smoke, the Ångström exponent showed the highest variability. The spread ranged from values slightly below 1 to values of about 2. Marine particles vary in size and can not be identified by the use of the particle linear depolarization ratio together with the Ångström exponent. Pollution consists of very small particles and is therefore characterized by high values of the Ångström exponent. Values of the Ångström exponent of about 1 and higher were frequently observed, indicating a huge frequency of occurrence of pollution during the campaign.

In conclusion, it can be stated that the particle linear depolarization ratio combined with the lidar ratio is the most relevant property for the classification of aerosol types and mixtures. With the Ångström exponent further information on the particles can be obtained, but it has a minor weight in regard to aerosol classification.

Values of the lidar ratio, particle linear depolarization ratio and Ångström exponent for all observed aerosol layers during the BACCHUS–Cyprus campaign are summarized in Table 6.3 and Table 6.4. For each aerosol type and mixture, the frequency of occurrence during the campaign is listed together with the calculated mean values and the range of the three intensive quantities at different wavelengths. For the calculation of the presented mean values and the standard deviation, the mean values of each aerosol layer, presented in the previous section, were taken into account. The range denotes the range of calculated mean values. If only one aerosol layer with a certain type or mixture was observed, only the calculated mean value of the layer together with the standard deviation was listed and the range was left out. Saharan dust, marine particles and pollution were the most present aerosol types in the atmosphere over Cyprus and frequently appeared as mixtures. Observed values are in good agreement with previous studies. The aerosol concentration was highest for pure Saharan dust, marine particles and mixtures of these two types. Pollution could only be detected in a rather low concentration, hence all calculated mean values for pollution should be handeled with care, even though they correlate well with previously observed values. Middle East dust solely appeared in the beginning of the campaign and was extensively discussed in Chapter 5. Three cases of smoke mixtures occured. Due to the high lidar ratio, it can be expected that the observed mixture of smoke, pollution and marine particles, as well as the mixture of smoke and pollution, contained a huge amount of smoke particles, whereas the mixture of Saharan dust and smoke obviously contained more dust than smoke, due to the high particle linear depolarization ratio and the low Ångström exponent.

Table 6.3: Summary of all observed aerosol types of the BACCHUS–Cyprus campaign, part 1: pure cases. Frequency of each aerosol type as well as mean value with standard deviation and range of the lidar ratio LR_λ, particle depolarization ratio δ_λ and Ångström exponent $\mathring{a}_{\alpha/\beta}$.

	Saharan Dust	Middle East Dust	Marine	Pollution
Frequency	3	1	13	6
LR_{355} [sr] mean	54±7	37±8	21±1	44±5
LR_{355} [sr] range	48 – 65	–	18 – 23	38 – 54
LR_{532} [sr] mean	52±4	36±6	24±2	50±7
LR_{532} [sr] range	47 – 58	–	19 – 26	37 – 71
δ_{355} mean	0.21±0.01	0.19±0.03	0.03±0.01	0.015±0.01
δ_{355} range	0.19 – 0.23	–	0.02 – 0.06	0.001 – 0.035
δ_{532} mean	0.25±0.01	0.22±0.02	0.04±0.01	0.02±0.02
δ_{532} range	0.24 – 0.26	–	0.02 – 0.08	0.001 – 0.06
$\mathring{a}_{\alpha(355/532)}$ mean	0.3±0.2	0.2±0.1	0.9±0.2	1.5±0.2
$\mathring{a}_{\alpha(355/532)}$ range	0.2 – 0.6	–	0.7 – 1.3	1.0 – 1.8
$\mathring{a}_{\beta(355/532)}$ mean	0.15±0.1	0.3±0.1	1.3±0.1	1.3±0.2
$\mathring{a}_{\beta(355/532)}$ range	0.06 – 0.3	–	0.9 – 1.5	0.7 – 1.8
$\mathring{a}_{\beta(532/1064)}$ mean	0.49±0.3	0.6±0.04	1.0±0.1	1.8±0.4
$\mathring{a}_{\beta(532/1064)}$ range	0.18 – 0.9	–	0.6 – 1.4	1.1 – 2.8

Table 6.4: Summary of all observed aerosol types of the BACCHUS–Cyprus campaign, Part 2: mixtures. Frequency of each mixture as well as mean value and range of the lidar ratio LR_λ, particle depolarization ratio δ_λ and Ångström exponent $å_{\alpha/\beta}$.

	Sah.+smoke	Sah.+poll.	Sah.+mar.	mar.+poll.
Frequency	1	6	10	12
LR_{355} [sr] mean	74±19	41±9	34±12	38±7
LR_{355} [sr] range	–	29 – 59	14 – 45	23 – 50
LR_{532} [sr] mean	65±13	46±5	32±7	36±6
LR_{532} [sr] range	–	38 – 51	23 – 43	26 – 50
δ_{355} mean	0.23±0.01	0.11±0.04	0.12±0.04	0.03±0.01
δ_{355} range	–	0.05 – 0.15	0.05 – 0.16	0.02 – 0.06
δ_{532} mean	0.25±0.01	0.12±0.06	0.16±0.02	0.04±0.01
δ_{532} range	–	0.06 – 0.2	0.08 – 0.25	0.03 – 0.07
$å_{\alpha(355/532)}$ mean	0.3±0.8	1.1±0.2	1.0±0.4	1.3±0.2
$å_{\alpha(355/532)}$ range	–	0.8 – 1.5	0.4 – 1.5	0.8 – 1.6
$å_{\beta(355/532)}$ mean	0.03±0.03	0.9±0.2	0.8±0.3	1.2±0.1
$å_{\beta(355/532)}$ range	–	0.4 – 1.2	0.3 – 1.3	0.6 – 1.7
$å_{\beta(532/1064)}$ mean	0.7±0.05	1.3±0.3	0.9±0.3	1.3±0.2
$å_{\beta(532/1064)}$ range	–	0.6 – 1.8	0.5 – 1.3	0.9 – 1.7

	ME mix	ME+mar.	ME+poll.	smoke+poll.	smoke+poll.+mar.
Frequency	1	3	1	1	1
LR_{355} [sr] mean	26±8	–	36±11	59±9	67±29
LR_{355} [sr] range	–	–	–	–	–
LR_{532} [sr] mean	30±11	33±5	31±7	62±10	71±23
LR_{532} [sr] range	–	27 – 40	–	–	–
δ_{355} mean	0.15±0.01	0.11±0.02	0.2±0.02	0.02±0.002	0.06±0.01
δ_{355} range	–	0.08 – 0.14	–	–	–
δ_{532} mean	0.19±0.01	0.17±0.0	0.2±0.01	0.035±0.001	0.09±0.01
δ_{532} range	–	0.17	–	–	–
$å_{\alpha(355/532)}$ mean	0.6±0.5	–	0.5±0.3	1.2±0.3	0.8±1.1
$å_{\alpha(355/532)}$ range	–	–	–	–	–
$å_{\beta(355/532)}$ mean	0.7±0.1	0.9±0.3	0.3±0.1	1.2±0.05	1.5±0.3
$å_{\beta(355/532)}$ range	–	0.6 – 1.3	–	–	–
$å_{\beta(532/1064)}$ mean	0.7±0.02	0.8±0.05	0.6±0.02	1.2±0.05	0.8±0.2
$å_{\beta(532/1064)}$ range	–	0.7 – 0.85	–	–	–

Chapter 7

Conclusion and Outlook

During the BACCHUS–Cyprus campaign in spring 2015, measurements with the multiwavelength–Raman–polarization lidar Polly^{XT} were performed. With this instrument, the backscatter and extinction coefficient are derived directly and independently. The lidar ratio, the Ångström exponent and the particle linear depolarization ratio can be calculated and give information about the observed scattering particles. Polly^{XT} is hence an appropriate tool to study aerosol optical properties.

Six weeks of lidar measurements took place at Cyprus, a location that is considered as one of the most polluted areas in the world (Weinzierl 2014). Different aerosol types and mixtures can appear. These were identified and analyzed within the context of this work. Late evening measurement periods were chosen for the application of the Raman–Lidar–Method. First, these measurement periods were analyzed with regard to aerosol layers and clouds. For all observed aerosol layers HYSPLIT backward trajectories were calculated to identify the origin of the detected air masses. Furthermore, information on fire activity and dust outbreaks was used for the determination of the different aerosol types and mixtures. With the Raman–Lidar–Method the backscatter and extinction coefficient were derived for each aerosol layer. Afterwards, the lidar ratio, the particle linear depolarization ratio and the Ångström exponent were calculated at different wavelengths and a mean value of these intensive quantities was determined for each aerosol layer.

Four measurement periods were chosen for detailed case studies, presented in Chapter 5. In this way, the above–described strategy could be demonstrated and an overview of typical aerosol conditions during the campaign was given. In addition, the aerosol optical properties of different aerosol types and mixtures could already be discussed in detail.

A statistical analysis was developed, including mean values of the three intensive quantities of all observed aerosol layers as well as the vertical extension of each aerosol layer. First, time series of these parameters were presented. During the campaign, the atmosphere over Cyprus was characterized by a huge amount of particles within the planetary boundary layer with a typical top height of about 2 km. Several elevated aerosol layers could be observed with a layer thickness between 0.4 and 5 km. Many elevated aerosol layers with a low concentration of aerosol particles were detected. In the time series of the aerosol optical properties no significant temporal trend could be noticed. All quantities showed a quite large variability, indicating an alternating occurrence of different aerosol types. In a next step, the lidar ratio, the particle linear depolarization ratio and the Ångström exponent for all aerosol layers were allocated to the different aerosol types and mixtures. Except for one mixture, all aerosol types and mixtures could be identified. Four almost pure aerosol types could be analyzed: Saharan dust, Middle East dust, marine particles and pollution. Saharan dust, marine particles and pollution showed the highest frequency of occurrence during the campaign. However, pure cases were rare. Most of the time, complex mixtures of dust, smoke, marine particles and pollution appeared. The aerosol optical properties of all aerosol types and mixtures that occurred during the campaign were discussed. All values were in good agreement with previous studies.
In the atmosphere over Cyprus, not only dust from the Saharan desert but also from deserts in the Middle East can be observed as already noticed by Nisantzi et al. (2015). During the campaign, only one pure case of Middle East dust occurred, showing a significantly lower lidar ratio and a slightly lower particle linear depolarization ratio compared to Saharan dust. For a meaningful comparison, a longer measurement campaign would be necessary. An entire year of measurements could make it possible to observe seasonal differences in the aerosol conditions in the region around Cyprus. Especially in summer, more cases of dust and smoke might be expected. The BACCHUS–Cyprus campaign was the first campaign with Polly^{XT}_ Noa. Some problems occurred that might be prevented in a further campaign. The near–range channel could not be used and due to the incomplete overlap between the receiver field of view and the laser beam, the extinction coefficient below 1 km was frequently biased and had to be left out.

Nevertheless, a valuable characterization of the aerosol optical properties of the observed aerosol types and mixtures was accomplished in this work. A further step could be the inspection of all cloud layers that appeared during the campaign to be able to study aerosol–cloud interactions. In this context, the ability of the different aerosol types to serve as CCN or IN could be investigated.

Bibliography

Albrecht, B. A. (1989). Aerosols, cloud microphysics, and fractional cloudiness. Science 245, 1227–1230.

Amiridis, V., D. Balis, S. Kazadzis, E. Giannakaki, A. Papayannis, and C. Zerefos (2005). Four years aerosol observations with a Raman lidar at Thessaloniki, Greece, in the framework of European Aerosol Research Lidar Network (EARLINET). Journal of Geophysical Research 110, D21203.

Ansmann, A., M. Riebesell, and C. Weitkamp (1990, July). Measurement of atmospheric aerosol extinction profiles with a Raman lidar. Optics Letters 15, 746–748.

Ansmann, A., U. Wandinger, M. Riebesell, C. Weitkamp, and W. Michaelis (1992). Independent measurement of extinction and backscatter profiles in cirrus clouds by using a combined Raman elastic–backscatter lidar. Applied Optics 31, 7113–7131.

ARD (2015). ARD tagesschau.de, 12.02.2015: Der Minsker Friedensplan (https://www.tagesschau.de/ausland/massnahmen-minsk-101˜_origin-441a34a8-6a5e-4f7b-b2f4-39693c063d46.html). Accessed: 27.03.17.

Baars, H., T. Kanitz, R. Engelmann, D. Althausen, B. Heese, M. Komppula, J. Preiler, M. Tesche, A. Ansmann, U. Wandinger, J. H. Lim, J. Y. Ahn, I. S. Stachlewska, V. Amiridis, E. Marinou, P. Seifert, J. Hofer, A. Skupin, F. Schneider, S. Bohlmann, A. Foth, S. Bley, A. Pfller, E. Giannakaki, H. Lihavainen, Y. Viisanen, R. K. Hooda, S. Pereira, D. Bortoli, F. Wagner, I. Mattis, L. Janicka, K. M. Markowicz, P. Achtert, P. Artaxo, T. Pauliquevis, R. A. F. Souza, V. P. Sharma, P. G. van Zyl, J. P. Beukes, J. Y. Sun, E. G. Rohwer, R. Deng, R. E. Mamouri, and F. Zamorano (2015). PollyNET: a global network of automated Raman-polarization lidars for continuous aerosol profiling. Atmospheric Chemistry and Physics Discussions 15, 27943–28004.

Baars, H., A. Ansmann, D. Althausen, R. Engelmann, B. Heese, D. Müller, P. Artaxo, M. Paixao, T. Pauliquevis, and R. Souza (2011, November). Aerosol profiling with lidar in the Amazon Basin during the wet and dry season. Journal of Geophysical Research (Atmospheres) 117, 21201.

BBC (2015). BBC NEWS, 02.03.2015: Iraq 'seizes districts from IS' in Tikrit advance (http://www.bbc.com/news/world-middle-east-31699632). Accessed: 27.03.17.

Draxler, R. and G. Rolph (2014). HYSPLIT (HYbrid Single-Particle Lagrangian Integrated Trajectory) Model access via NOAA ARL READY Website (http://ready.arl.noaa.gov/HYSPLIT.php). NOAA Air Resources Laboratory, Silver Spring M.D.

Engelmann, R., T. Kanitz, H. Baars, B. Heese, D. Althausen, A. Skupin, U. Wandinger, M. Komppula, I. S. Stachlewska, V. Amiridis, E. Marinou, I. Mattis, H. Linn, and A. Ansmann (2016). The automated multiwavelength Raman polarization and water–vapor lidar PollyXT: the neXT generation. Atmospheric Measurement Techniques 9, 1767–1784.

Freudenthaler, V., M. Esselborn, M. Wiegner, B. Heese, M. Tesche, A. Ansmann, D. Müller, D. Althausen, M. Wirth, A. Fix, G. Ehret, P. Knippertz, C. Toledano, J. Gasteiger, M. Garhammer, and M. Seefeldner (2009). Depolarization ratio profiling at several wavelengths in pure Saharan dust during SAMUM 2006. Tellus Series B 61, 165–179.

Ginoux, P., J. M. Prospero, T. E. Gill, N. C. Hsu, and M. Zhao (2012). Global-scale attribution of anthropogenic and natural dust sources and their emission rates based on MODIS Deep Blue aerosol products. . Reviews of Geophysics 50, RG3005.

Groß, S., M. Esselborn, B. Weinzierl, M. Wirth, A. Fix, and A. Petzold (2013). Aerosol classification by airborne high spectral resolution lidar observations. Atmospheric Chemistry and Physics 13(5), 2487–2505.

Groß, S., V. Freudenthaler, M. Wiegner, J. Gasteiger, A. Geiß, and F. Schnell (2012). Dual-wavelength linear depolarization ratio of volcanic aerosols: Lidar measurements of the Eyjafjallajökull plume over Maisach, Germany. Atmospheric Environment 48, 85–96.

Groß, S., M. Tesche, V. Freudenthaler, C. Toledano, M. Wiegner, A. Ansmann, D. Althausen, and M. Seefeldner (2011). Characterization of Saharan dust, marine aerosols and mixtures of biomass–burning aerosols and dust by means of multi-wavelength depolarization and Raman lidar measurements during SAMUM 2. Tellus Series B 63, 706–724.

Hamidi, M., M. R. Kavianpour, and Y. Shao (2013). Synoptic analysis of dust storms in the Middle East. Asia–Pacific Journal Of Atmospheric Sciences 49, 279–286.

http://bacchus env.eu/ (2017). BACCHUS Website. Accessed: 20.02.17.

http://ready.arl.noaa.gov/HYSPLIT.php (2017). HYSPLIT Trajectory Model. Accessed: 27.04.17 and 08.05.17.

https://firms.modaps.eosdis.nasa.gov/firemap/ (2017). FIRMS Web Fire Mapper provided by NASA. Accessed: 24.03.17.

https://worldview.earthdata.nasa.gov (2017). NASA Worldview. Accessed: 28.03.17.

Huffingtonpost (2015). The Huffington Post, 12.04.2015: Lessons From the Second Battle of Tikrit: March 2–April 4 2015 (http://www.huffingtonpost.com/joseph-v-micallef/lessons-from-the-second-b_b_7049430.html). Accessed: 27.03.17.

Illingworth, A. J., H. W. Barker, A. Beljaars, M. Cecca ldi, H. Chepfer, N. Clerbaux, J. Cole, J. Delano, C. Domenech, D. P. Donovan, S. Fukuda, M. Hirakata, R. J. Hogan,

A. Huenerbein, P. Kollias, T. Kubota, T. Nakajima, T. Y. Nakajima, T. Nishizawa, Y. Ohno, H. Okamoto, R. Oki, K. Sato, M. Satoh, M. W. Shephard, A. Velzquez-Blzquez, U. Wandinger, T. Wehr, and G. J. van Zadelhoff (2015). THE EARTHCARE SATELLITE The Next Step Forward in Global Measurements of Clouds, Aerosols, Precipitation, and Radiation. American Meteorological Society.

IPCC (2007). Climate change 2007: The scientific basis. contribution of working group i to the fourth assessment report of the intergovernmental panel on climate change. Cambridge University Press 996 pp.

IPCC (2013). Fifth assessment report of the intergovernmental panel on climate change. Cambridge University Press.

IRAQINEWS (2015). IRAQI NEWS, 14.04.2015: Security forces, tribal fighters liberate 2 areas in al-Karma (http://www.iraqinews.com/iraq-war/security-forces-tribal-fighters-liberate-2-areas-al-karma/). Accessed: 27.03.17.

Kanitz, T. (2012). Vertical distribution of aerosols above the Atlantic Ocean, Punta Arenas (Chile) and Stellenbosch (South Africa) – Characterization, solar radiative effects and ice nucleating properties. Ph. D. thesis, Faculty of Physics and Geoscience, University of Leipzig.

Klett, J. D. (1981). Stable analytical inversion solution for processing lidar returns. Applied Optics 20, 211–220.

MOA (2017a). Department of Forests, Cyprus: Forest Fires (https://www.moa.gov.cy/moa/fd/fd.nsf/DMLprotection_en/DMLprotection_en). Accessed: 08.02.17.

MOA (2017b). Department of Meteorology, Cyprus: Climate of Cyprus (http://www.moa.gov.cy/moa/ms/ms.nsf/DMLcyclimate_en/DMLcyclimate_en). Accessed: 07.02.17.

MOA (2017c). Department of Meteorology, Cyprus: Meteorological Report for March 2015 (http://www.moa.gov.cy/moa/MS/MS.nsf/All/1622E95F98BC40CBC2257E4B003FE798/$file/GAZ_Mar2015_UK.pdf)
and April 2015 (http://www.moa.gov.cy/moa/MS/MS.nsf/All/FAD47275F541F38BC2257E7C0037D0B7/$file/GAZ_Apr2015_UK.pdf). Accessed: 07.02.17.

NASA (2015). Fires in Sierra Leone March 2015 (https://www.nasa.gov/content/goddard/fires-in-sierra-leone-march-2015). Accessed: 27.03.17.

Nicolae, D., A. Nemuc, D. Müller, C. Talianu, J. Vasilescu, L. Belegante, and A. Kolgotin (2013). Characterization of fresh and aged biomass burning events using multiwavelength raman lidar and mass spectrometry. Journal of Geophysical Research: Atmospheres 118, 2956–2965.

Nisantzi, A., R. E. Mamouri, A. Ansmann, and D. G. Hadjimitsis (2014). Injection of mineral dust into the free troposphere during fire events observed with polarization lidar at Limassol, Cyprus. Atmospheric Chemistry and Physics.

Nisantzi, A., R. E. Mamouri, A. Ansmann, G. L. Schuster, and D. G. Hadjimitsis (2015). Middle East versus Saharan dust extinction-to-backscatter ratios. Atmospheric Chemistry and Physics.

Papayannis, A., R. E. Mamouri, V. Amiridis, S. Kazadzis, C. Perez, G. Tsaknakis, P. Kokkalis, and J. M. Baldasano (2009). Systematic lidar observations of Saharan dust layers over Athens, Greece in the frame of EARLINET project (2004–2006). Annals of Geophysics 27, 3611–3620.

Prospero, J. M., P. Ginoux, O. Torres, S. E. Nicholson, and T. E. Gill (2002). Environmental characterization of global sources of atmospheric soil dust identified with the NIMBUS 7 Total Ozone Mapping Specrometer (TOMS) absorbing aerosol product. Reviews of Geophysics 40, 1002.

Rajeev, K., V. Ramanathan, and J. Meywerk (2000). Regional aerosol distribution and its long–range transport over the Indian Ocean. Journal of Geophysical Research 105, 2029–2043.

Rao, P. G., M. Al–Sulaiti, and A. H. Al–Mulla (2001). Winter shamals in Qatar, Arabian Gulf. Weather 56, 444–451.

Reuters (2015). Reuters WORLD NEWS, 08.03.2015: Rebel sniper kills Ukrainian serviceman despite ceasefire - military (http://uk.reuters.com/article/uk-ukraine-crisis-casualties-idUKKBN0M40EC20150308). Accessed: 27.03.17.

Sassen, K. (2005). Lidar: Range–resolved optical remote sensing of the atmosphere, Chapter Polarization lidar, pp. 19–40. Springer.

Seifert, P. (2010). Dust–related ice formation in the troposphere – A statistical analysis based on 11 years of lidar observations of aerosols and clouds over Leipzig. Ph. D. thesis, Faculty of Physics and Geoscience, University of Leipzig.

Tesche, M., A. Ansmann, D. Müller, D. Althausen, R. Engelmann, V. Freudenthaler, and S. Groß (2009). Vertically resolved separation of dust and smoke over Cape Verde using multiwavelength Raman and polarization lidars during Saharan Mineral Dust Experiment 2008. Journal of Geophysical Research 114, D13202.

Tesche, M., A. Ansmann, D. Müller, D. Althausen, I. Mattis, B. Heese, V. Freudenthaler, M. Wiegner, M. Esselborn, G. Pisani, and P. Knippertz (2009). Vertical profiling of Saharan dust with Raman lidars and airborne HSRL in southern Morocco during SAMUM. Tellus Series B 61, 144–164.

Tesche, M., S. Gross, A. Ansmann, D. Müller, D. Althausen, V. Freudenthaler, and M. Esselborn (2011). Profiling of Saharan dust and biomass-burning smoke with multiwavelength polarization Raman lidar at Cape Verde. Tellus Series B 63, 649–676.

Toledano, C., V. E. Cachorro, A. Berjon, A. M. de Frutos, M. Sorribas, B. A. de la Morena, and P. Goloub (2007). Aerosol optical depth and Angstrom exponent climatology at El Arenosillo AERONET site (Huelva, Spain). Q. J. R. Meteorol. Soc..

Twomey, S. (2007). Pollution and the planetary albedo. Atmospheric Environment 41, 120–125.

UCMC (2015). UKRAINE CRISIS media center, 07.03.2015: Andriy Lysenko: Ukrainian Armed Forces did not suffer any casualties in 24 hours (http://uacrisis.org/19521-andrijj-lisenko-54). Accessed: 27.03.17.

Wandinger, U. (2005). Lidar - Range–resolved optical remote sensing of the atmosphere, Chapter Introduction to lidar, pp. 1—18. Springer Science + Business Media Inc.

Washington, R., M. Todd, N. J. Middleton, and A. S. Goudie (2003). Dust–storm source areas determined by the Total Ozone Monitoring Spectrometer and surface observations. Annals of the Association of American Geographers 93, 297–313.

Weinzierl, B. (2014). ERC Starting Grant– Research Proposal for A–LIFE (Absorbing aerosol layers in a changing climate: aging, lifetime, and dynamics). (http://www.pa.op.dlr.de/aercare/).

Zhu, A., V. Ramanathan, F. Li, and D. Kim (2007). Dust plumes over the Pacific, Indian, and Atlantic Oceans: Climatology and radiative impact. Journal of Geophysical Research 112, D16208.

List of Figures

1.1 Aerosol transport to Cyprus (overview) 2

2.1 Meteorological Report for March and April 2015 for Nicosia, Cyprus 6
2.2 Fire Activity in the region around Cyprus, 10–day periods 7
2.3 Dust sources in the region around Cyprus 9
2.4 Saharan Dust Outbreaks during the experiment 11
2.5 Middle East Dust Outbreaks during the experiment 12

3.1 BACCHUS–Cyprus campaign – Measurement location 14
3.2 Installation of instruments at Nicosia during the BACCHUS–Cyprus campaign 15
3.3 Measurement Calendar of observations with Polly^{XT} at Nicosia during the BACCHUS–Cyprus campaign 16
3.4 The optical setup of Polly^{XT}_ OCEANET 18

4.1 Aerosol Classification: Lidar ratio and particle linear depolarization ratio at 355 nm, Illingworth et al., 2015 26

5.1 Time–height plot of the range–corrected signal at 1064 nm (top) and the 532 nm volume depolarization ratio (bottom) for March 2015 (Nicosia, Cyprus) 29
5.2 Time–height plot of the range–corrected signal at 1064 nm (top) and the 532 nm volume depolarization ratio (bottom) for April 2015 (Nicosia, Cyprus) 30
5.3 Time–height plot of the range–corrected signal at 1064 nm (07.03.2015, 18.00–00.00 UTC Nicosia, Cyprus) 32
5.4 HYSPLIT backward trajectories arriving at Nicosia, Cyprus on March 7, 2015, 20.00 UTC 33
5.5 Profiles of the backscatter and extinction coefficient, lidar ratio, Ångström exponent and particle linear depolarization ratio (07.03.2015, 19.00–21.00 UTC, Nicosia, Cyprus) 34

5.6 Time–height plot of the range–corrected signal at 1064 nm (09.03.2015, 18.00–00.00 UTC Nicosia, Cyprus) . . . 36
5.7 HYSPLIT backward trajectories arriving at Nicosia, Cyprus on March 9, 2015, 19.00 UTC . . . 37
5.8 Profiles of the backscatter and extinction coefficient, lidar ratio, Ångström exponent and particle linear depolarization ratio (09.03.2015, 18.00–22.30 UTC, Nicosia, Cyprus) . . . 38
5.9 Time–height plot of the range–corrected signal at 1064 nm (07.04.2015, 12.00–00.00 UTC Nicosia, Cyprus) . . . 39
5.10 HYSPLIT backward trajectories arriving at Nicosia, Cyprus on April 7, 2015, 19.00 UTC . . . 40
5.11 Profiles of the backscatter and extinction coefficient, lidar ratio, Ångström exponent and particle linear depolarization ratio (07.04.2015, 18.00–19.30 UTC, Nicosia, Cyprus . . . 41
5.12 Time–height plot of the range–corrected signal at 1064 nm (09.04.2015, 18.00–00.00 UTC Nicosia, Cyprus) . . . 42
5.13 HYSPLIT backward trajectories arriving at Nicosia, Cyprus on April 9, 2015, 19.00 UTC . . . 43
5.14 Profiles of the backscatter and extinction coefficient, lidar ratio, Ångström exponent and particle linear depolarization ratio (09.04.2015, 18.30–21.00 UTC, Nicosia, Cyprus) . . . 44

6.1 Time Series– Aerosol layer vertical extension . . . 49
6.2 Time Series– Backscatter coefficient . . . 50
6.3 Time Series– Extinction coefficient . . . 51
6.4 Time Series– Lidar ratio . . . 52
6.5 Time Series– Depolarization ratio . . . 53
6.6 Time Series– Ångström exponent . . . 54
6.7 Aerosol Characterization: lidar ratio vs. particle linear depolarization ratio . 56
6.8 Aerosol Characterization: lidar ratio vs. Ångström exponent . . . 58
6.9 Aerosol Characterization: particle linear depolarization ratio vs. Ångström exponent . . . 59

List of Tables

2.1 Desert dust layer statistics for 49 outbreaks (2010–2013), Nisantzi et al., 2015 13

6.1 Observed aerosol layers during the BACCHUS–Cyprus campaign (March 2015) 47
6.2 Observed aerosol layers during the BACCHUS–Cyprus campaign (April 2015) 48
6.3 Summary of all observed aerosol types of the BACCHUS–Cyprus campaign, part 1: pure cases 61
6.4 Summary of all observed aerosol types of the BACCHUS–Cyprus campaign, Part 2: mixtures 62

List of Abbreviations

AERONET	Aerosol Robotic Network
AOT	Aerosol Optical Thickness
ARL	Air Resources Laboratory (NOAA)
ASL	above sea level
BACCHUS	Impact of Biogenic versus Anthropogenic emissions on Clouds and Climate: towards a Holistic UnderStanding
CCN	Cloud Condensation Nuclei
Det	Detector
EARLINET	European Aerosol Research Lidar Network
Fig.	Figure
FIRMS	Fire Information for Resource Managment System (Earthdata)
GDAS	Global data assimilation system
HYSPLIT	Hybrid Single–Particle Lagrangian Integrated Trajectory
IN	Ice Nuclei
IPCC	Intergovernmental Panel on Climate Change
laser	Light Amplification by Stimulated Emission of Radiation
lc	low concentration
lidar	light detection and ranging
mar	marine
ME	Middle East
MOA	Ministry of Agriculture, Rural Development and Environment, Cyprus
MODIS	Moderate Resolution Imaging Spectroradiometer
mol	molecules
NASA	National Aeronautics and Space Administration
NOA	National Observatory of Athens
NOAA	National Oceanic and Atmospheric Administration (United States of America)

par	particles
PBL	planetary boundary layer
poll	pollution
Polly	portable lidar
Sah.	Saharan
SD	Standard Deviation
SHG	Second Harmonic Generator
Tel	Telescope
THG	Third Harmonic Generator
TROPOS	Leibniz Institute for Tropospheric Research
UTC	Universal time coordinated
vol	volume

Selbstständigkeitserklärung

Ich, Clara Kaduk, Matrikel–Nr. 2143166, versichere hiermit, dass ich meine Masterarbeit mit dem Thema

> Characterization of the optical properties of complex aerosol mixtures
> observed with a multiwavelength–Raman–polarization lidar during the
> 6–weeks BACCHUS campaign in Cyprus in spring 2015

selbständig verfasst und keine anderen als die angegebenen Quellen und Hilfsmittel benutzt habe, wobei ich alle wörtlichen und sinngemäßen Zitate als solche gekennzeichnet habe. Die Arbeit wurde bisher keiner anderen Prüfungsbehörde vorgelegt und auch nicht veröffentlicht.

Leipzig, den 12.07.2017

Clara Kaduk